Technical University Munich

Proton Production in Pion-Nucleus Collisions at 1.7 GeV/c at HADES

Master thesis

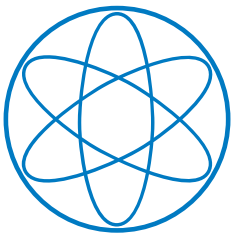

Thesis submitted in fulfilment of the requirements for the degree of Master of Science
at Dense and Strange Hadronic Matter
at Physics Department

Author:
Verena Eiblmeier
Matriculation number:
03692560
Munich, March 11, 2020

Reviewer:
Prof. Dr. Laura Fabbietti
Supervisor:
Dr. Joana Wirth
Dr. Steffen Maurus

Abstract

This thesis represents the study of proton production in $\pi^- + A$ collisions at an incident beam momentum of 1.7 GeV/c using the HADES spectrometer at GSI. The data was recorded in 2014. To identify and reconstruct protons, a graphical selection, which is based on the $\beta - p$ relation, is applied. Afterwards, the experimental data are corrected due to HADES detector acceptance and efficiency. The number of corrected protons for π^- + C reactions is $N^C_{\text{corr}} = 5.51741 \cdot 10^7$ and for π^- + W is $N^W_{\text{corr}} = 1.11617 \cdot 10^8$. The extracted proton production cross sections are on the one hand for π^- + C reaction $\Delta\sigma^C_p = 133127 \pm (3)^{\text{stat}} \pm (20569)^{\text{sys}} \pm (^{+20918}_{-17115})^{\text{norm}}\ \mu b$ and on the other hand for π^- + W reaction $\Delta\sigma^W_p = 1560370 \pm (192)^{\text{stat}} \pm (563353)^{\text{sys}} \pm (^{+245188}_{-200609})^{\text{norm}}\ \mu b$. Furthermore, a comparison to two state-of-the-art transport models, GiBUU and UrQMD, shows a similar behavior and a reasonable agreement at forward rapidities for the proton production cross section as a function of rapidity. Moreover, the comparison to HARP data shows a minor incoming beam momentum dependency at low transverse momenta which vanishes at higher transverse momenta.

Contents

1 Introduction

More than one century ago Joseph Thomson discovered the electron. That also marked the starting point to discover the inner structure of atoms. In 1919 Ernest Rutherford detected the proton and predicted the neutron which was discovered by James Chadwick 13 years later. Together with the photon, a lot of phenomena can be described. Since that, the improvement of accelerators, particle detectors and statistics leaded to an entire zoo of particles which are connected through one theory: The Standard Model of particle physics [11].

1.1 The Standard Model

The Standard Model describes in principle the constituents of matter and the interaction among them. It is based on the fact, that all matter is made of particles which interact with each other by exchanging various particles associated with the fundamental forces. All fermions have spin 1/2. They are divided into two categories, quarks and leptons. The six types of quarks indicated as violet in Fig. 1.1 are up, down, charm, strange, top and bottom. Based on charge and mass they belong to three different families. The first family consists of up and down quark out of what stable matter is built of. For example, protons consist of two up and one down quark which results in proton charge equal to $+1$. The others are leptons which are illustrated in green in Fig. 1.1. Leptons are also divided into three families containing e^+, e^-, μ^+, μ^-, τ^+, τ^- and their corresponding neutral (anti)neutrinos ν_e, ν_μ, ν_τ.

In nature four types of fundamental interactions are known to exist which are the gravitational, the electromagnetic, the strong and the weak. Each of them can be mathematically described as a field. On particle physic scales, the gravitational force is not significant and is excluded in the Standard Model [11]. The three other forces are discrete quantum fields and their interactions are mediated by elementary particles which are virtual exchange bosons with spin 1 and they are described in the Standard Model.

The electromagnetic force acts on charged particles. It is carried by massless photons, has therefore an infinite scale and creates electric, as well as magnetic fields. This force is responsible for the attraction potential in atomic nuclei which holds atoms together. The

weak force acts on all particles of the Standard Model which is for example responsible for the $\beta-$decay. It is carried by the three massive exchange bosons $W^{\pm}$ and Z^0 which results in short range of the weak interaction compared to the electromagnetic. Above very high temperatures the exchange bosons of electromagnetic and weak interactions are essentially identical and the two theoretical descriptions merge to the unified electroweak interaction as Sheldon Glashow, Abdus Salam and Steven Weinberg predicted [11]. The strong force acts on (anti)quarks which carries the colors (anti)blue, (anti)green and (anti)red. In nature there is just color neutrality which appears through the combination of either three quarks, or one quark antiquark pair. So quarks can form baryons on the one hand and mesons on the other hand. Baryons are made out of three quarks, for example the proton consists of two up quarks and one down quark. Mesons are constructed by one pair of quark and antiquark like for example pions ($|\pi^+\rangle = \left|u\bar{d}\right\rangle$, $|\pi^-\rangle = |d\bar{u}\rangle$, $|\pi^0\rangle = 1/\sqrt{2}[|u\bar{u}\rangle - \left|d\bar{d}\right\rangle]$). The strong force is carried by eight different massless gluons and make it possible for quarks to form nucleons and then they can further form the atomic nuclei. Gluons are able to interact among themselves and therefore the range of the strong force is in the order of $10^{-15}\,m$ which corresponds to the proton radius.

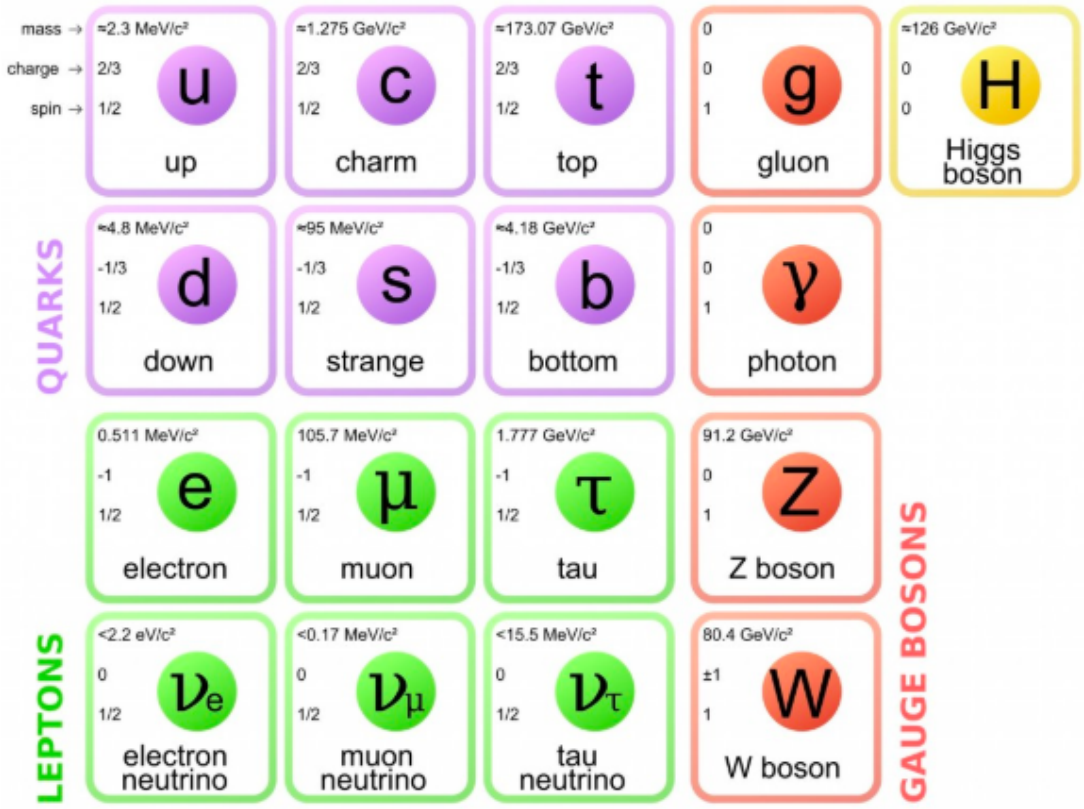

Figure 1.1: Illustration of the Standard Model of particle physics [22].

The last missing piece which was predicted by the Standard Model is the neutral Higgs boson (indicated in yellow in Fig. 1.1) with spin 0 and $m = 125\,\mathrm{GeV/c^2}$, which was discovered at CERN in 2012. Nearly 50 years ago it was predicted that through introducing a scalar field (Higgs field) the spontaneous symmetry braking in Gauge theories, could be explained. With applying this Higgs field on the electroweak theory, it leads to the generation of the high and different masses of the $W^{\pm}$ and Z^0. The scalar field also gives mass to the fundamental fermions through the Yukawa interaction [10].

1.2 Hadron Mass Generation

All stable matter is built out of protons which are the lightest stable particles. Compared to the mass of its components, which sums up to $9.1\,\mathrm{MeV/c^2}$, the rest mass $m_p = 938.272\,\mathrm{MeV/c^2}$ of the proton is much larger [23]. This missing mass can be explained by introducing the spontaneous breaking of chiral symmetry. In the chiral effective field theory, the degrees of freedom are hadrons or quarks. Its fundamental symmetry is the $SU(3)_L \otimes SU(3)_R$, where the chirality of left- and right-handed hadrons is conserved and the quark masses go to zero in the chiral limit. This means, in the interaction among quarks via gluon exchange, right-handed quarks stay right-handed quarks as well as left-handed quarks stay left-handed quarks. The vacuum, which is populated by scalar quark-antiquark pairs $\langle 0|\,\bar{q}q\,|0\rangle$, called chiral condensate, does not share the invariance under $SU(3)_L \otimes SU(3)_R$ chiral transformation. If a q_R/q_L interacts with the chiral condensate like $q_L + \bar{q}_L q_R = q_R$, one can see that the ground state does not vanish. So, going to the ground state (vacuum), the expectation value $\langle 0|\,\bar{q}q\,|0\rangle$ is not zero and as a consequence this symmetry is broken. Including the quark masses, the spontaneous breaking of the chiral symmetry generates hadron masses. So the missing mass of the proton is generated through the binding energy of the strong force which holds the components of the nucleus together [24].

With increasing temperature and density, the expectation value is decreasing until its restoration (Fig. 1.2). This means that at high temperatures and high densities the hadron mass is predicted to change. For this prediction there are many experimental searches. Large Hadron Collider (LHC) (indicated in yellow in Fig. 1.2) can reach high temperatures whereas experiments located at Heavy-Ion Synchrotron (SIS) 18 (indicated in green in Fig. 1.2) are able to reach higher densities. Originally, High-Acceptance DiElectron Spectrometer (HADES) located at SIS 18 studied the in-medium modification of light vector mesons [1].

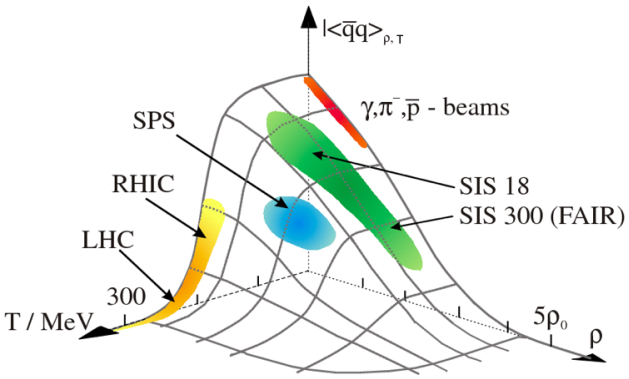

Figure 1.2: Expectation value of the chiral condensate as a function of the temperature T and nuclear density ρ/ρ_0. The different experiment regions are indicated [13].

1.3 Structure and Goal of this Thesis

The study of hadron production has a long history in high-energy particle, nuclear, and cosmic ray physics. The most basic physical observables, for example in high-energy hadron-hadron collisions, are the absolute yields and the transverse momentum (p_t) spectra. They can be used to improve parameters of hadronic event generators in state-of-the-art transport models. In this work, the double-differential proton production cross-section in $\pi^- + \mathrm{C}$ and $\pi^- + \mathrm{W}$ is presented.

Proton production in pion nucleus reactions at kinetic energies around a few AGeV occurs mostly through inelastic scattering and through the strong decay of short-lived baryonic resonances (e.g. $N^\star$, $\Delta(1232)$).

Figure 1.3 shows the full analysis chain, to obtain the corrected proton yield and hence the double-differential cross-section of protons. Chapter 2 gives a short overview of the pion beam facility and the relevant components of the HADES detector system. An important step is to simulate events with two different transport models (GiBUU and UrQMD). A general overview of transport models is given in the first part of Chapter 3. In the second part of Chapter 3, the necessary steps to simulate the detector influence on particles are described. At this point, the simulated data as well as the experimental data have the same structure. The first part in Chapter 4 describes the full analysis procedure which is applied to the experimental data as well as to both simulation data. The analysis procedure starts with the event selection (Section 4.1.1), the proton identification and reconstruction (Section 4.1.2) and the acceptance and efficiency correction (Section 4.1.3). The second transport model (UrQMD) is used to prove the model independence of the corrected experimental yield. The error calculation is performed in Section 4.1.4.

To extract the yield in unmeasured transverse momentum p_t regions, a Boltzmann extrapolation is applied (Section 4.1.5). As a last step in the analysis procedure, the absolute normalization is necessary to obtain the proton production cross-section (Section 4.1.6). Besides, the obtained results are compared to transport model predictions and the HARP data. The HARP Collaboration performed extensive measurements of the inclusive double-differential proton production cross-section in various pion-nucleus reactions [8]. The varying incoming beam momenta for the HARP data are in between ($3\,\mathrm{GeV/c} - 15\,\mathrm{GeV/c}$). The different target materials are Be, C, Cu, Sn, Ta and Pb. One motivation for the HARP experiment was to make a systematic study of precise hadron production for $\pi + \mathrm{A}$ and $p + \mathrm{A}$ over a wide transverses momentum and angle range to validate and improve hadron production models. This work provides proton production of two different nuclei in terms of double-differential cross-sections at a lower incident pion beam momentum ($1.7\,\mathrm{GeV/c}$). So the existing double-differential proton production cross-section in $\pi^- + \mathrm{C}$ reaction of the HARP data could be enlarged to lower incident beam momenta. Moreover, the double-differential proton production in $\pi^- + W$ of this work expands the different target materials.

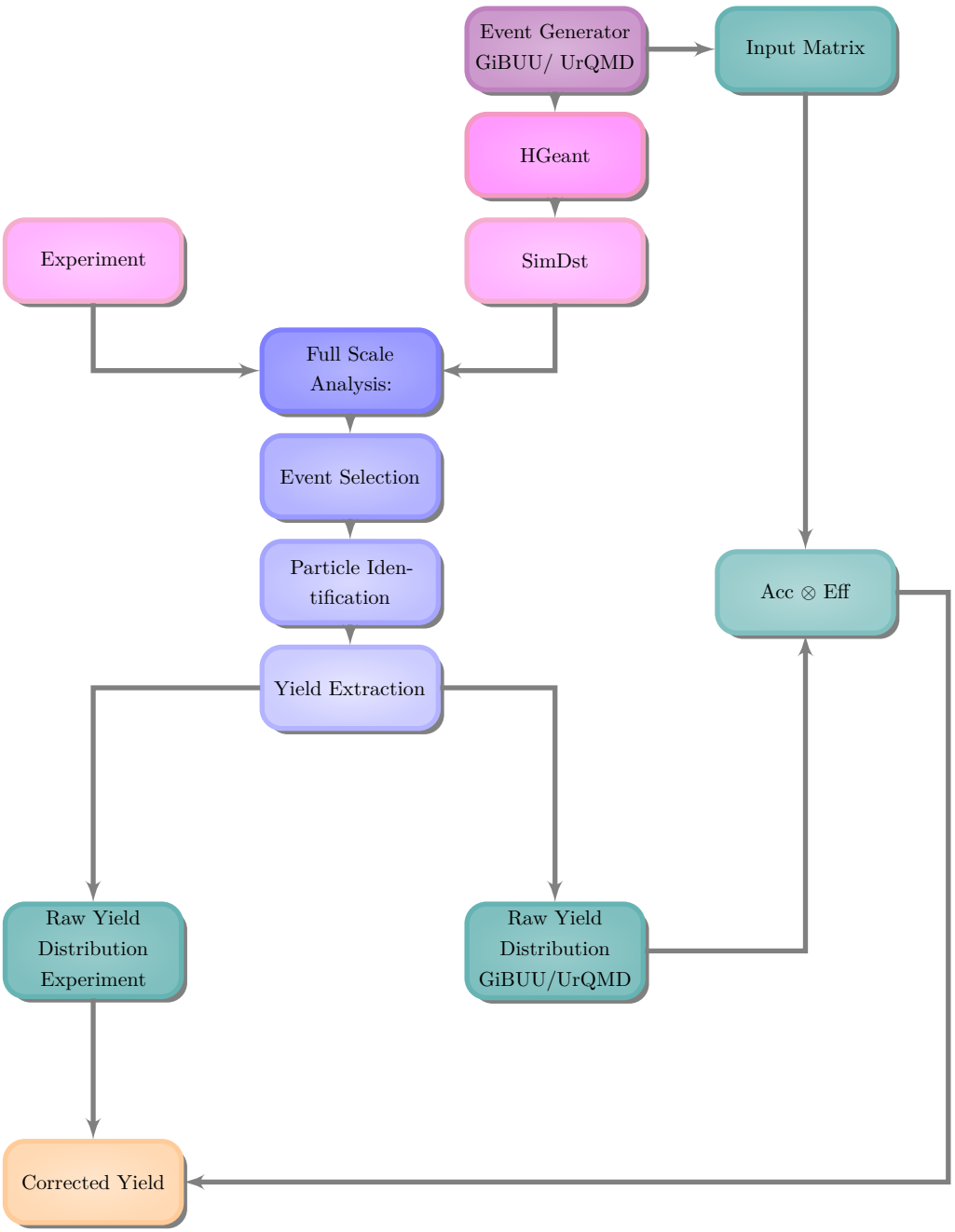

Figure 1.3: Schematic of the complete analysis chain which is employed to get the experimental corrected proton yield. The simulated events of GiBUU/UrQMD (dark violet) have to be processed through simulation tools including HGeant and SimDST to create events which has the same structure and losses as the experimental data (magenta). Afterwards, both the experimental and simulated data are analyzed (blue) in the same way. The Acc⊗Eff matrix is needed to extract the corrected experimental yield (orange).

2 The HADES Experiment

HADES is a magnetic spectrometer which is located at the GSI Helmholtzzentrum für Schwerionenforschung in Darmstadt (Germany). It is a fixed target experiment designed for various collisions, e.g. nucleus-nucleus, proton-proton, proton-nucleus, or pion-nucleus collisions. Originally it was designed to study medium modifications of light vector mesons e.g. ρ, ω, ϕ in elementary and heavy-ion-induced reactions. Equally important is their electromagnetic decay branch into e^+e^- pairs [2]. The possibility to have HADES in combination with a secondary pion beam provides the unique opportunity to study hadron and dielectron production in pion-proton collisions in various beam momenta from 0.656 GeV/c until 800 GeV/c and pion-nucleus collisions at 1.7 GeV/c [1].

2.1 Pion Beam Facility

In 2014 an experimental campaign was carried out by the HADES Collaboration impinging a negatively charged pion beam at 1.7 GeV/c beam momentum on carbon and tungsten targets. The secondary pion beam can be produced by the collision of high intensity protons or heavy-ion beams with a thick production target. These proton- or ion beams up to energies of 4.5 GeV and 2 AGeV are delivered from a synchrotron of maximum 18 Tm rigidity located at the GSI accelerator complex. Studies with pion beams in [12] showed that the largest pion current with beam momenta between 0.656 GeV/c and 1.7 GeV/c at HADES is possible by impinging ^{12}C or ^{14}N ion beams onto a 10 cm thick Be target. For technical reasons a primary ^{14}N beam with intensities of about $0.8 - 1.0 \cdot 10^{11}$ ions/spill was used [19]. In this collision, together with the pions also other particles are produced. Positive pion beams are contaminated with positrons, positive muons, positive kaons, protons and nuclear fragments. The contamination by electrons, negative muons and kaons of a negative charged pion beam is minor and was estimated to be below a few percentages [19]. In order to get a clean beam, dipoles select pions along the beam-line towards HADES through their deflection angle. Quadrupole magnets focus the beam [12]. A schematic drawing of the pion beam-line and its different elements to transport the beam from the production target to HADES is visualized in Fig. 2.1.

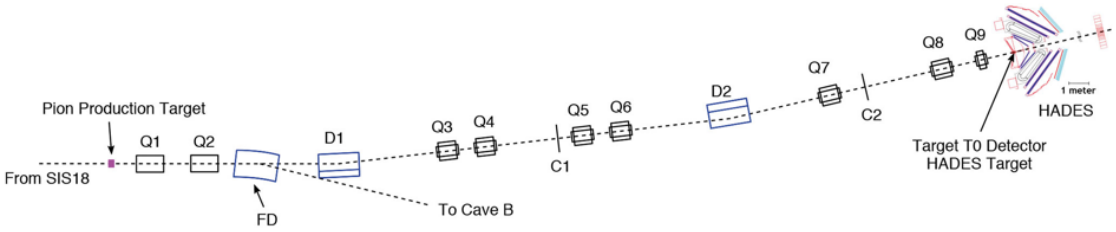

Figure 2.1: Schematic overview of the beam line between the pion production target and the HADES cave. The dipole magnets(D), quadrupoles (Q), tracking detectors (C1, C2) and the target-T_0 detector are indicated. The FD dipole which is used to direct the beam to cave B is shown as well [1].

Due to a huge spread out of the beam in momentum and position, the beam-line acceptance is around $\Delta p/p \approx 8\%$. To achieve a better momentum resolution of 5% [1] , a secondary beam diagnostic system, called CERBEROS, was installed. It consists of two tracking stations C_1 and C_2 (see Fig. 2.1) and the target-T_0 detector (see Fig. 2.1), which will be explained in Section 2.2. C_1 is located after the production target in between quadrupole magnets Q_4 and Q_5. C_2 is located behind the second dipole D_2, closer to the target. The target-T_0 detector, which is located 2 cm in front of the target, allows to optimize the beam profil and the generation of a fast timing signal for trigger purposes and time-of-flight particle identification. It was developed to offer online beam monitoring and for reconstruction of momentum, as well as the position for pions [25].

2.2 Detector System

The HADES detector system is built out of six identical sectors. Superconducting magnetic coils produce a toroidal magnetic field. The spectrometer covers polar angles between $18° \leq \theta \leq 85°$. A schematic layout of the HADES detector system is displayed in Fig. 2.2 in which all parts are sketched. To reconstruct the momentum, the deflection angle of particle trajectories arising from four hit positions in MDCs located before and after the magnetic coils is measured. Behind the MDCs, the META system consisting of RPC and TOF is located on the one hand to improve the track reconstruction with an extra hit information and on the other hand to perform the time-of-flight measurement. The first level trigger (LVL1) selects events with a predefined charged particle multiplicity [2]. A more detailed description of the individual detector systems, which are necessary for the hadron analysis, will be presented in the following.

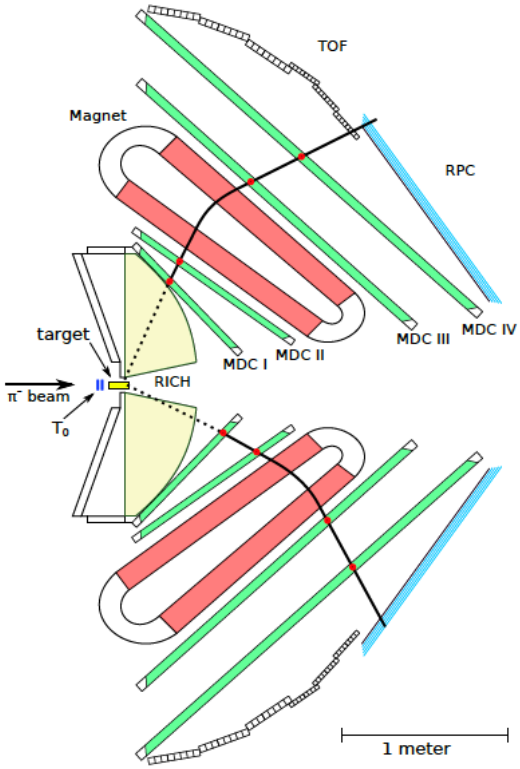

Figure 2.2: HADES detector and its important components [18].

Target-T_0 Detector

Coming along from the pion beam direction, the secondary pion beam impacts first on the target-T_0 detector. It is located 2 cm in front of the HADES target and detects the reaction start time t_0 for the time-of-flight measurement. The detector, which was particularly designed for the pion beam campaign, consists of nine diamond sensors and is pictured in Fig. 2.3. Each is based on mono-crystalline diamond material which is produced by the chemical vapor deposition (CVD) process. This detector has to fulfill a good timing precision $\delta t \leq 100$ ps. The obtained time resolution was about $\delta t \approx 250$ ps. The detector didn't reach the expected time precision due to the extensive pick-up noise in the target-T_0 detector. However, a considerable amount of off-vertex reactions could be suppressed on the trigger level. Timing signals from the CERBEROS beam tracking detector layers were used to suppress pile-up and multi hit events in the tracking stations on the LVL1 trigger level. [1].

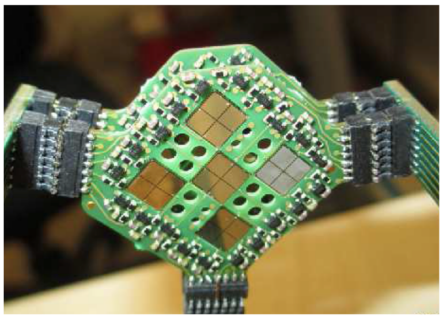

Figure 2.3: Photography of the target T_0 detector [1].

Target

The employed targets are sketched in Fig. 2.4 consisting of three segments indicated in yellow. The distance between the individual segments is 18 mm. The red boxes represent the edges of the RICH detector. The area around the target is nearly field free. The target material properties are summarized in Table 2.1.

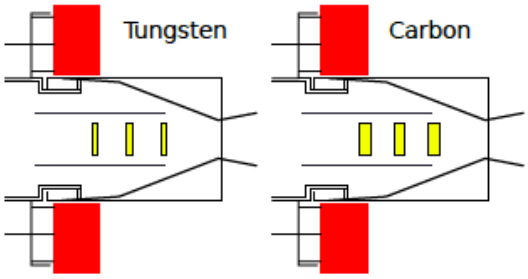

Figure 2.4: Schematic drawings of the solid target consisting of tungsten (left) and carbon (right) separated into three segments (yellow) and the edges of the RICH detector (red).[26] [18].

Table 2.1: Material and target properties of carbon and tungsten targets.

Target	N_{segment}	A	d_{segment} [mm]	$\varnothing$ [mm]	ρ [g/cm^3]
C	3	12.011	7.2	12	1.85
W	3	183.84	2.4	12	19.3

Magnet

The superconducting magnet which consists of six coils surrounding the beam axis is used for track reconstruction. Its toroidal field geometry provides a field free region around the target. Its maximum field strength is obtained at the sector edge and reaches up to 3.6 T. To cool down the coils, they are surrounded by a liquid nitrogen shield [2].

Mini Drift Chambers

The other components of the magnet spectrometer to reconstruct the trajectory of particles are 24 trapezoidal planar MDCs (Mini-Drift Chambers), which are arranged in six identical sectors. Each of the four detector planes (MDC *I-IV*) has a different orientation (see Fig. 2.5 left panel) to optimize the spatial resolution. Each detector plane is subdivided into six sectors. Whereas all MDC chamber models feature 6 field wire layers with a different orientation. In every single sector, two MDC planes (MDC *I*, *II*) are in front of the superconducting magnet and two others (MDC *III*, *IV*) are located behind [2].

Charged particles passing the drift cells in the chamber ionize the gas along their trajectory. The resulting free electrons are multiplied in an electric field through avalanche effects while drifting towards sense wires. The induced signal then can be read out. On basis of this signal, the hit position in the MDC can be reconstructed. After passing the two MDCs, the charged particles are deflected by the toroidal magnetic field as visualized in Fig. 2.5 (right panel). To estimate the bending direction and the radius of the curvature, measurements of the particles track in front (A, B) and behind (C, D) the magnet are necessary. Based on these measurements the determination of the particle track points, the path length, the particles momentum and charge is possible with a resolution of $1 - 4\%$. For particle identification one needs also the velocity out of the time-of-flight measurement. The explanation is coming up next.

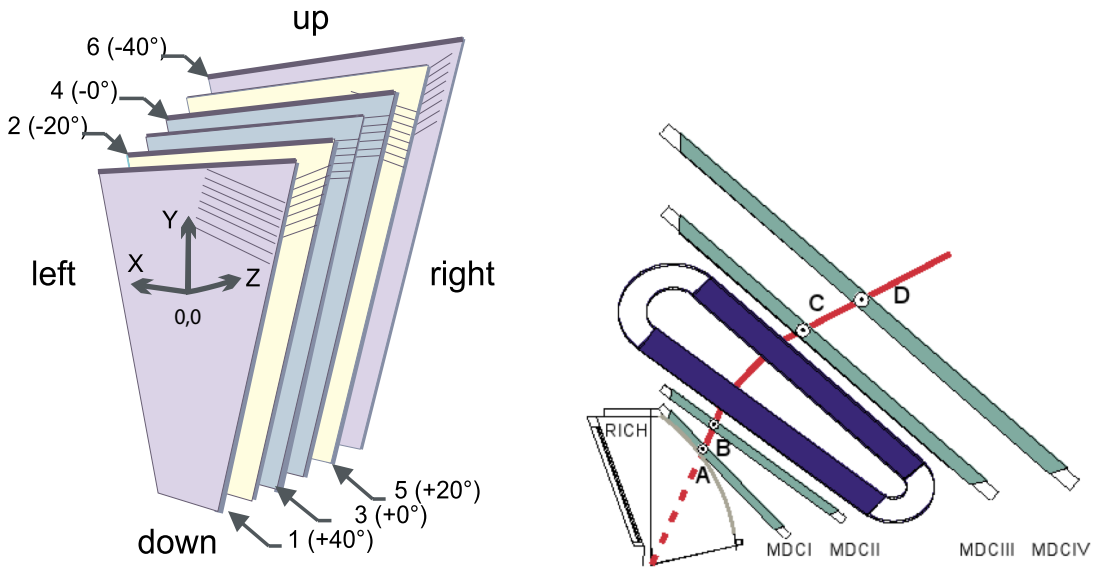

Figure 2.5: Left: Schematic illustration of a MDC chamber. Each chamber consists of six trapezoidal layers with different field wire orientations [2]. Right: Image of an exemplary charged particle track through the magnet spectrometer consisting of magnetic coil and four MDCs [26].

META System

The Multiplicity Electron Trigger Array (META) consists of two time-of-flight detectors (TOF) and the Resistive Plate Chamber (RPC). Its main applications are a fast determination of the charged-particle multiplicity of an event basis for the trigger decision and the time-of-flight measurement in combination with the target-T_0 detector. Both detectors are located behind MDC IV.

The TOF detector covers large polar angles from 44° to 85°. Like the whole spectrometer, also TOF is divided into six identical sectors. Each sector consists of eight modules, which are constructed of eight scintillator rods (in total 384) with PMTs on both ends [2]. Particles crossing the scintillator excite the material. By emitting photons, the excited material returns back to the ground state. The photons are amplified and transformed into an electrical signal in the PMTs. The arrival time with a resolution of $\sigma_t \approx 150\,\text{ps}$ and the amplitudes of the signal in the PMTs allow to extract the time-of-flight and the deposited energy of the particle. These information are used for the particle identification [2].

The lower polar angle region in between 18° and 45° is covered by the RPC detector. As well as TOF, RPC holds the six-folder-structure of HADES. However, the RPC has a better time resolution, which is below $\sigma_t \approx 100\,\text{ps}$. It is built up by various amounts of independent detector cells (Fig. 2.6 left panel). Each individual cell (Fig. 2.6 right panel) is made of alternating aluminium and glass plates, which are surrounded by an aluminium box to avoid cross-talk. The gap between the two parallel electrode plates is filled with gas, as illustrated in Fig. 2.6 (right panel). The aluminium layers which represent these electrodes have a high voltage difference between them to create a homogeneous electric drift field in the gas volume. An electrically charged particle traversing the RPC detector ionizes gas molecules along its trajectory. In the homogeneous drift field the electrons are accelerated towards the anode, creating an avalanche of charge carriers (so-called gas amplification), which induces an electrical signal in the electrodes.

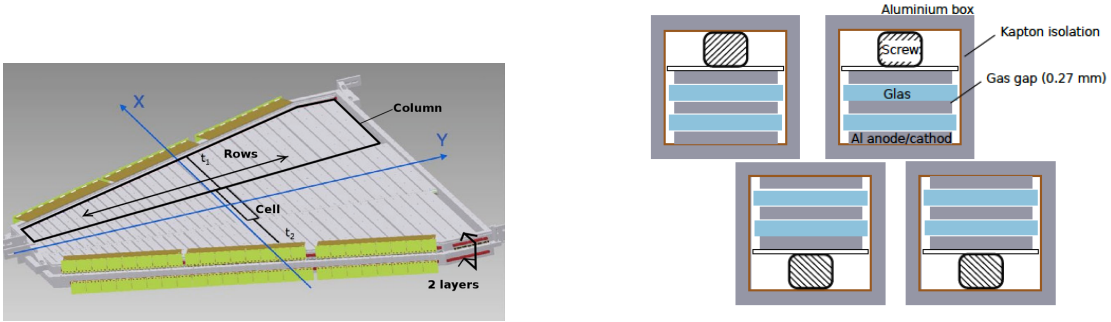

Figure 2.6: Left: Schematic drawing of one sector of the RPC detector [21]. Right: Illustration of one RPC cell [18].

Central Trigger System

If incoming beam particles interact with the target the reaction products produce signals which are used as input for the Central Trigger System (CTS). The CTS which consists of a Central Trigger Unit (CTU) and a Matching Unit (MU) produces the trigger signals. The basic principle of the two level trigger system is shown in Fig. 2.7. The CTU generates digital trigger information and can handle several types of triggers. This information is then transported to the individual Detector Trigger System (DTS). Using this concept, the read out boards send only the fraction of events which matches one of the trigger decisions (LVL1, LVL2) to the event builder [14].

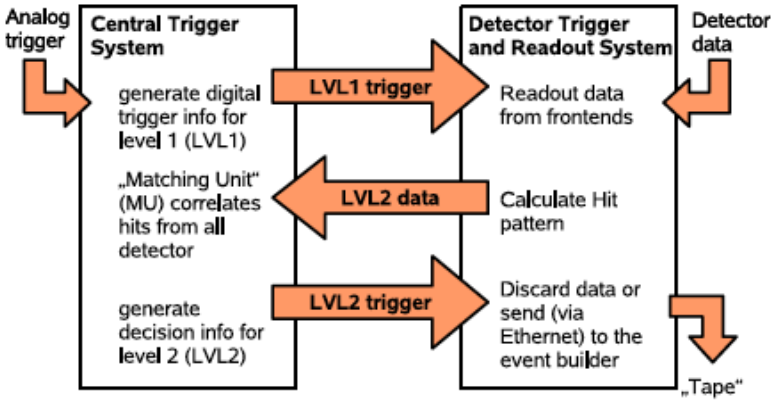

Figure 2.7: Basic principle of the HADES two-level trigger system: The trigger sources are sampled by the central trigger system (CTS). Trigger information is transported to the individual detector trigger systems (DTS). Data with a positive trigger decision are transported to the event builder (EB) [14].

The first level trigger (LVL1) is based on a fast determination of the charged particle multiplicity to minimize random noise events in the data [1]. The LVL1 selects only events if the charged particle multiplicity is $M \geq 2$ in the META System in combination with a hit in the target-T_0 detector. If the LVL1 trigger condition is fulfilled the trigger signal goes to all detectors.

The LVL2 trigger decision is based on the real time e^+e^- identification. In the experimental pion beam campaign this trigger decision was not used [1].

3 Simulations

In general, simulations have a significant importance for the interpretation of the experimental data in hadron-hadron collisions at intermediated energies. In this Chapter, first of all, relevant aspects of transport models will be shortly discussed followed by introducing two specific models, GiBUU and UrQMD. Since the GiBUU and UrQMD models are also used to apply efficiency and acceptance corrections to the experimental data, they have to be processed through various simulation tools to mimic the same influences and losses as the experimental data. These individual steps are explained in the second part of this Chapter.

3.1 Transport Model Calculations

In experimental hadron-hadron collisions the information of final-state particles are integrated over the whole time evolution of the collision process. To learn about the reaction dynamics, transport models are used. Transport model descriptions are based on processes at the microscopic level.

Their major advantage is that they follow the entire time evolution of the reaction. That means they are able to simulate the physical reaction from the initial state until the particle production at any chosen time interval. Besides this, they are based on experimental input (e.g. cross-sections) to simulate realistic reactions.

The GiBUU and UrQMD transport models are based on the non-relativistic BUU (Boltzmann-Uehling-Uhlenbeck) equation (Eq. 3.1.1), which describes the space-time evolution of the single-particle phase space density $f(\vec{r}, \vec{p}, t)$ influenced by a collision term I_{coll}. The collision term includes gain and loss terms according to scattering and decay processes. Also Pauli blocking is included in the collision term I_{coll}. Each particle species is represented by one differential equation [27] [4]

$$\left(\frac{\partial}{\partial t} + \frac{\vec{p}}{m} \cdot \nabla_r + \vec{F} \cdot \nabla_p\right) f(\vec{r}, \vec{p}, t) = I_{\text{coll}}. \tag{3.1.1}$$

The BUU equation (Eq. 3.1.1) is a non-linear integral-differential equation which cannot

be solved analytically or in a direct numerical way. A common approach for example is the test-particle ansatz (GiBUU) [27].

3.1.1 GiBUU

The Giessen Boltzmann-Uehling-Uhlenbeck (GiBUU) model, which was originally developed to describe heavy-ion collisions is a transport model for hadron-, photon-, electron-, neutron- and heavy-ion-induced reactions. The suitable energy range for the GiBUU transport model starts at a few 10 MeV and goes up to 40 GeV [15][9].

To solve the BUU equation (Eq. 3.1.1) the test-particle ansatz is used in GiBUU. In this approach, the single-particle distribution function $f(\vec{r}, \vec{p}, t)$ is replaced by a huge number of test particles N (Eq. 3.1.2) which follow the shape of a $\delta-$function [27]

$$f(\vec{r}, \vec{p}, t) \rightarrow \sum_{i}^{N} \delta(\vec{r} - \vec{r}_i(t))\delta(\vec{p} - \vec{p}_i(t)). \tag{3.1.2}$$

In the GiBUU test-particle ansatz the assumption is made, that the many-body-system behaves like a classical fluid on microscopic space-time scales [9]. The initial state is either in agreement with the experimental conditions (hadron-nucleus and heavy-ion collisions) or is determined by external models (photon, electron and neutrino nucleus reactions). In low and mediated energy ranges, the particle production is created through a resonance model. Here hadrons originate from resonance decays. The relevant degrees of freedom are mesons and baryons, which are propagated through a mean field potential and scatter according to cross-sections. In total 34 mesons and 90 baryons are included. At higher energies (> 3 GeV) quarks and gluons become the degrees of freedom. Here GiBUU switches to the string model PYTHIA including string fragmentation which generates particles at the quark level by breaking up strings [9].

3.1.2 UrQMD

The Ultra relativistic Quantum Molecular Dynamik (UrQMD) model is a transport theory based on the QMD approach. The Quantum Molecular Dynamics model is a N-body theory based on a covariant propagation of all hadrons on classical trajectories. A significant difference to the test-particle ansatz is the representation of the particles. Each nucleon is represented by a coherent state in form of a Gaussian wave package (Eq. 3.1.3) which is characterized by six time-dependent parameters $\vec{r}_i$ (space coordinates) and $\vec{p}_i$ (momentum coordinates). In Eq. 3.1.3 L is related to the extension of the Gaussian

wave package and the simplification $\hbar = c = 1$ is used [3]

$$\phi_i(\vec{r};\, \vec{r}_i\, \vec{p}_i, t) = \left(\frac{2}{L\pi}\right)^{3/4} exp\{-\frac{2}{L}(\vec{r} - \vec{r}_i(t))^2 + i\vec{p}_i(t)\vec{r}\}. \tag{3.1.3}$$

The total wave function Φ in Eq. 3.1.4 is the direct product of all coherent states (Eq. 3.1.3)[3]

$$\Phi = \prod_i \phi_i(\vec{r};\, \vec{r}_i\, \vec{p}_i, t). \tag{3.1.4}$$

The collisions in the QMD simulations are limited to binary collisions (two-body level) and performed in a point-particle sense similar to BUU models. The total cross-section of hadron-hadron collisions is estimated with the help of the geometrical cross-section. The collision of two particles is taking place, if the minimum distance d between two particles satisfies (Eq. 3.1.5). The latter determined the total cross-section σ_{tot}, which is dependent on the isospins of colliding particles, their flavor and the center-of-mass energy [4]

$$d < \sqrt{\frac{\sigma_{\mathrm{tot}}}{\pi}}. \tag{3.1.5}$$

In UrQMD the available energy ranges from the SIS ($\sqrt{s} \approx 2\,\mathrm{GeV}$) region up to RHIC energy ($\sqrt{s} \approx 200\,\mathrm{GeV}$). The collision term includes more than 50 baryon species like N, Δ or Y resonances with masses up to $2.25\,\mathrm{GeV/c^2}$ and 45 mesons. At high energies, quarks and gluons cannot be neglected anymore and hence UrQMD switches also to a string model like GiBUU [4].

3.1.3 Absolute Normalisation of Simulated Data

To obtain the proton production cross-section in order to perform a comparison to experimental measurements the results of the transport model calculations have to be absolutely normalized. The absolute normalization is in general based on the geometrical cross-section σ_{geom} (Eq. 3.1.6), in which b_{max} describes the maximum impact factor

$$\sigma_{\mathrm{geom}}[\mathrm{mb}] = \frac{\pi \cdot b_{\mathrm{max}}^2}{10}. \tag{3.1.6}$$

The factor 10 is needed to convert fm^2 to mb.

GiBUU

For GiBUU the production cross-section σ is given by Eq. 3.1.7

$$\sigma = \frac{\sigma_{\mathrm{geom}}}{N_{\mathrm{files}} \cdot N_{\mathrm{ensembles}}} \cdot N. \tag{3.1.7}$$

Here the geometrical cross-section σ_{geom} is calculated (Eq. 3.1.6) on the basis b_{max} which is provided by simulations. In Eq. 3.1.7 N is the number of events where a reaction took place, N_{files} is the number of simulated files and $N_{\text{ensembles}}$ stands for the number of particles in each file.

UrQMD

The production cross-section σ of UrQMD is given in a similar way (Eq. 3.1.7). However, the geometrical cross-section σ_{geom} is directly provided in UrQMD. As well as for GiBUU, N_{files} is the whole amount of simulated files and $N_{\text{ensembles}}$ the amount of simulated particles for each file.

3.2 Simulation Tools

To correct the data for acceptance and efficiency effects, which will be explained in detail in Section 4.1.3 a full-scale simulation is necessary. The results of transport models, e.g. GiBUU and UrQMD, have to be processed through a chain of different tools displayed in Fig. 1.3 (magenta), which will be discussed in the following. The second transport model, in this work UrQMD is required to perform a self-consistency check, which will also be explained in Section 4.1.3, to make sure that the correction method is model independent.

HGeant

The HGeant framework is a simulation tool based on the CERN software Geant 3.21 [16], which contains the complete HADES detector setup. In order to simulate the particle interaction with the detector material, particles which are produced by GiBUU and UrQMD, are propagated through HGeant. Relevant physical processes are for example secondary collisions, scattering processes and energy loss in the detectors.

SimDST

The information provided by HGeant has to go through SimDST (Simulated Data Summary Table) level, in which the detector response is considered and finally the simulated particle tracks are reconstructed like real data. The evaluated particle momenta are stored. After this step the simulated data has the same structure as the experimental data. Hence, the same analysis procedure can be applied, what will be explained in Section 4.1. With this, the matrices for acceptance and efficiency corrections (Acc$\otimes$Eff see Section 4.1.3) can be obtained in order to provide unbiased yield distributions for the physical interpretation.

4 Inclusive Proton Production

The inclusive proton (p) production in π^-+C and π^-+W collisions at a beam momentum of 1.7 GeV/c is presented in this chapter. It contains the complete analysis procedure as well as the obtained final results namely the double-differential distribution. Besides, the comparison to state-of-the-art transport models and the HARP data is discussed.

4.1 Analysis Procedure

The large statistic allows to perform a double-differential analysis in a set of independent kinematic variables in the laboratory frame. The initial set of kinematic independent variables is the transverse momentum p_t in combination with the rapidity y.

The transverse momentum p_t (Eq. 4.1.1) is defined perpendicular to the beam axis (z-axis) and thus carries the information about the interaction process

$$p_t = \sqrt{p_x^2 + p_y^2}. \tag{4.1.1}$$

The rapidity y of a particle (Eq. 4.1.2) can be expressed as

$$y = \frac{1}{2}\ln\left(\frac{E + p_z}{E - p_z}\right) = \frac{1}{2}\ln\left(\frac{1 + \beta\cos(\theta)}{1 - \beta\cos(\theta)}\right) \tag{4.1.2}$$

where p_z denotes the particle momentum along the beam axis, E its energy and θ is the polar angle. Regarding the rapidity there is a differentiation into three regions: Beam- (forward), target- (backward) and mid-rapidity. The target rapidity is used for $y = 0$, whereas $y \to \infty$ is called beam rapidity.

In the $p_t - y$ phase space the transverse momentum ranges from $0 - 1000$ MeV/c ($\Delta p_t = 40$ MeV/c) and the rapidity is between 0 and 1.2 ($\Delta y = 0.1$). This analysis allows to extract a cross-section as a function of the rapidity $\sigma(y)$.

4.1.1 Event Selection

To make sure that in this analysis only reactions are considered in which the secondary π^- beam interacts with the target, the recorded events have to fulfill certain event selection criteria. The initial point of the event selection is ,that a hit was registered in the target-T_0 detector and all events comply with the LVL1 physical trigger conditions (Section 2.2). The first level trigger (LVL1) selects only events with a charged particle multiplicity $M \geq 2$ in the META system in combination with a hit in the target-T_0 detector. In this analysis the following event selection criteria were applied:

NoPileUp

An important criterion is to reject so called pile-up events which leads to a wrong determination of the reaction time t_0 and thus to an incorrect time-of-flight measurement. A pile-up is the case in which multiple pions are registered in the target-T_0 detector in the time window for the selection of a single event. To reject pile-up events a multiplicity of one is reconstructed in the target-T_0 detector in the time window starting form $-5\,\text{ns}$ until $15\,\text{ns}$.

goodClustVert

After excluding pile-up events the selected event has at least to satisfy the condition to have not less than one track in the inner MDC I/II. Also a selection on the χ^2 of the reconstructed vertex bigger than zero is applied and its position in z-direction should be greater than $-160\,\text{mm}$.

Multiplicity

In the experimental data only events are included that satisfy the LVL1 trigger conditions, as mentioned before.The simulation has to go through the same selection procedure as the measured data. Hence, the selection criterion is also applied to the simulated data.

Primary vertex reconstruction

To ensure that only events which interact with the target are taken, selections on the primary vertex are considered. The vertex is calculated by the distance of closest approach to all the tracks registered in MDC and META. This method requires at least two fully reconstructed tracks. In the left panel in Fig. 4.1 the $z-$component of the primary vertex distribution is indicated in black for the experimental data. Three peaks are visible which belong to the three segments of the target. The two red lines display the primary vertex cut in $z-$direction corresponding to range of $z = -80\,\text{mm}$ and $z = 5\,\text{mm}$.

The dashed gray distribution for a GiBUU simulation is in good agreement with the experimental primary vertex distribution. The primary vertex resolution in z-direction is $\sigma_{zPV} \approx 4.7\,\text{mm}$ [26]. Furthermore, the primary vertex distribution in the $xy-$plane was exploited. The resolution for the primary vertex in x-(y-)direction is $\sigma_{xPV} \approx 3.1\,\text{mm}$ ($\sigma_{yPV} \approx 2.6\,\text{mm}$). Indicated by the black circle in Fig. 4.1 b) the vertex cut in $xy-$plane with $R = \sqrt{x^2 + y^2} < 20\,\text{mm}$ is shown.

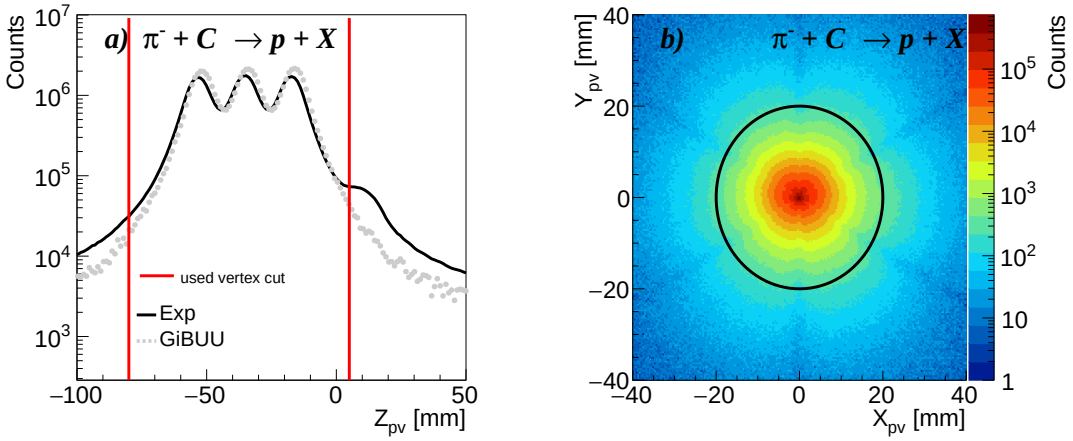

Figure 4.1: Primary vertex distributions in $z-$direction a) with the selected region indicated by the red lines. b) Primary vertex distribution in $xy-$plane including the selected area (resembled as a black circle).

The effect of the mentioned event selection criteria in Fig. 4.2 are visualized for the experimental data as well as the GiBUU simulation (Chapter 3). For both, $\pi^- + \text{C}$ and $\pi^- + \text{W}$ reactions, the looses are quite similar. For example, the experimental data ($\pi^- + C$) drop down to 74% including all event selection criteria while for the GiBUU simulated data goes to 77%.

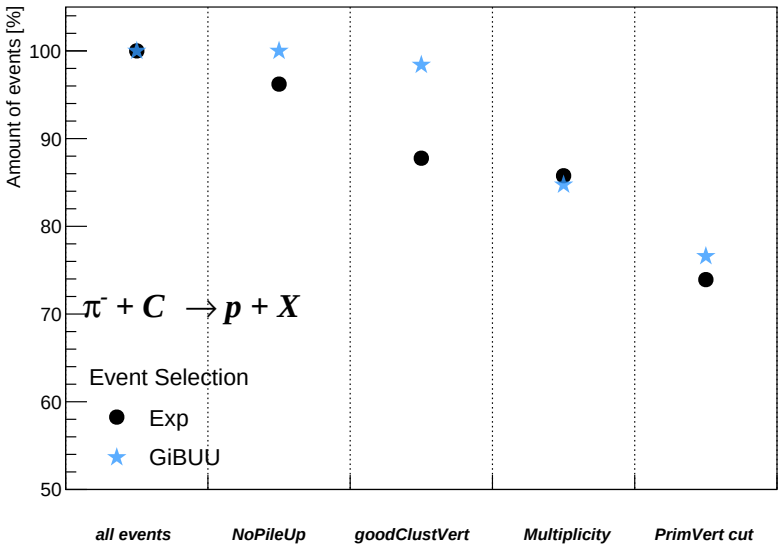

Figure 4.2: Individual event selection criteria and their remaining events in %, starting from the complete amount of registered events going through all selection criteria like NoPileUp, goodClustVert, Multiplicity and Primary vertex selection.

4.1.2 Proton Identification and Reconstruction

The next step of the proton analysis is the proton identification. The particle identification is performed separately for RPC and TOF to account for the different resolutions. One possibility to identify protons is based on the β-momentum relation ($c = 1$)

$$\beta(p) = \frac{p}{E} = \sqrt{\frac{\vec{p}^2}{m^2 + \vec{p}^2}} \tag{4.1.3}$$

with the energy E, defined as $E = \sqrt{\vec{p}^2 + m^2}$ and m denotes the proton mass ($m_p = 938.272\,\mathrm{MeV/c^2}$) [23].

Figure 4.3 shows the $p - \beta$ distribution for RPC including all positive charged particles assuming that all positive particles are protons. The step at about 300 MeV/c could be caused by the energy loss and magnetic field correction for proton candidates. As the analysis is focusing only on protons the same corrections were applied to all particles. So here it was assumed that all particles are protons. The future proton analysis is not impacted by this fact. The theoretical β-values for p, π^+ and d are indicated by the black curves. For low momenta the theoretical β-value for π^+ does not match with the experimental data. This can be attributed to the fact that the momentum correction for

protons was applied assuming that the pion is a proton. As only protons are considered in the further analysis this has no influence on the presented inclusive proton analysis.

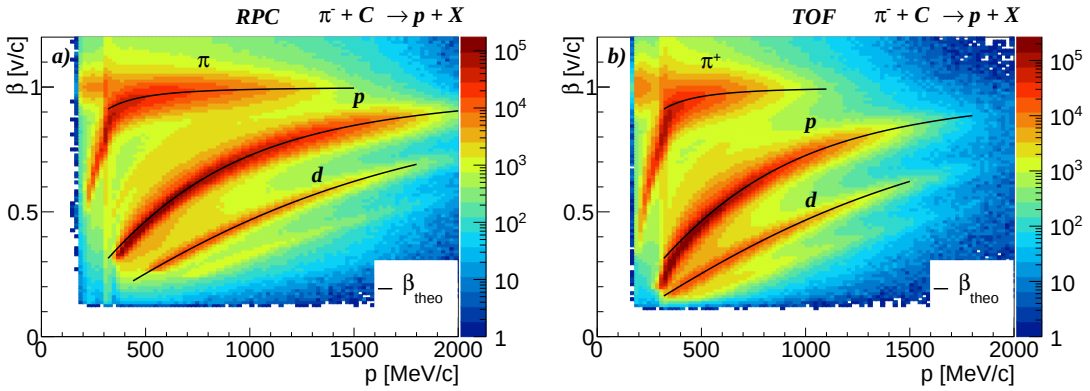

Figure 4.3: The $p-\beta$ spectrum for RPC (a)) and TOF (b)) detectors containing positively charged particles with a momentum correction for protons. The theoretical β curves for p, π^+ and d are indicated by the black curves.

To identify the protons, the $\beta - p$ distribution was projected on the velocity axis in momentum intervals of 20 MeV/c. Figure 4.4 shows the β distribution of p, π^+ and d in an exemplary momentum interval (720 − 740 MeV/c). To describe the β-distribution for p, π^+ and d simultaneously a Gaussian distribution was adopted for each particle species in order to extract the mean μ and the resolution σ of the proton distribution in each momentum slice. Hence, the entire distribution was adapted with the sum of these three Gaussian functions (Eq 4.1.4). As demonstrated in Fig. 4.4 the measured distribution is almost background free, hence no addition function is needed.

$$f(x) = A_p \cdot e^{-\frac{1}{2}\cdot\left(\frac{x-\mu_p}{\sigma_p}\right)^2} + A_{\pi^+} \cdot e^{-\frac{1}{2}\cdot\left(\frac{x-\mu_{\pi^+}}{\sigma_{\pi^+}}\right)^2} + A_d \cdot e^{-\frac{1}{2}\cdot\left(\frac{x-\mu_d}{\sigma_d}\right)^2} \tag{4.1.4}$$

In Figure 4.4 the experimental β distributions for π^+, p, d together with their theoretical β values indicated by dashed vertical lines are shown. Besides of that, the individual Gaussian fits and the combined fit are presented. In β-distribution in the momentum range from 720 MeV/c to 740 MeV/c in RPC the mean value μ_p of the individual Gaussian fit for protons is $\mu_p = 0.61$, while its resolution is $\sigma_p = 0.02$.

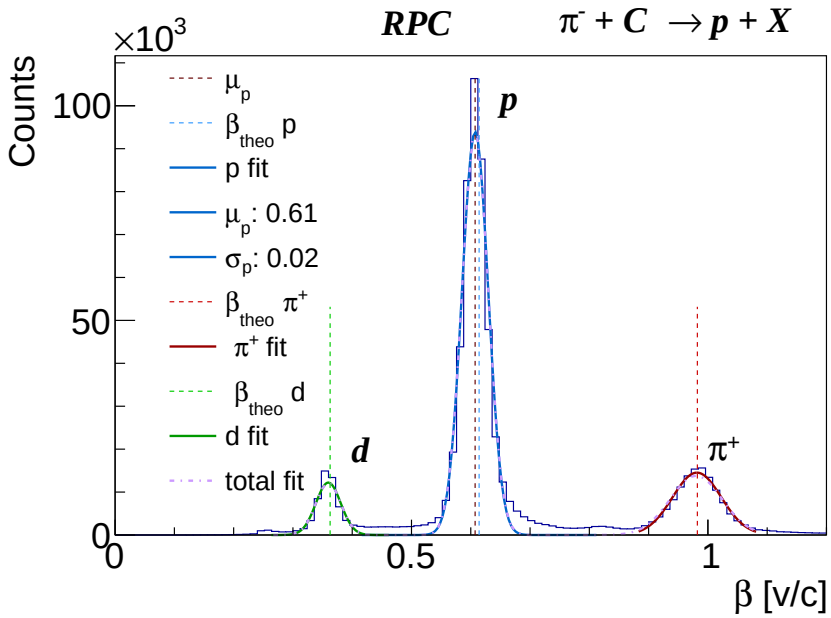

Figure 4.4: β-distributions of p, π^+, and d in the momentum range from 720 MeV/c to 740 MeV/c in RPC. The individual Gaussian fits and the combined fit (magenta) are included. The combined fit consists of the three Gaussian fits for d (green), p (blue) and π^+ (red). The dashed lines belong to the theoretical β-values.

Furthermore, the mean (μ_p) and width (σ_p) of the $\beta-$distribution extracted from the single proton Gaussian fit are compared to the values from the combined fit. The mean values agree perfectly over the selected range. Moreover, the mean μ_p compared to the theoretical β for the protons is also in good agreement over the selected range within in average about 1% (Fig. 4.5 a)). Given that the proton peak is isolated it is possible to take μ_p and σ_p of the Gaussian individual fit instead of the combined fit. In addition, the resolution σ at low/high momenta is more stable for the individual Gaussian fit. Since, for low momenta the $\beta-$distribution becomes asymmetric due to a non-linear correlation between β and momentum p, the assumption of a Gaussian is not fully justified. Hence, the resolution σ_p as a function of the momentum shows deviations from the monotone behavior (Fig. 4.5 b)). To obtain the resolution σ_p over the entire momentum range, the distribution was adapted with a second-order polynomial function. Thus, the σ_p values from the polynomial fit have been further used.

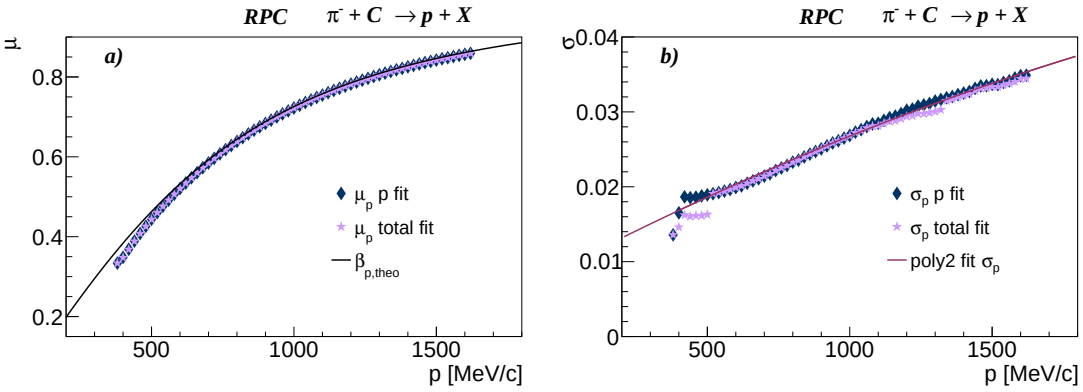

Figure 4.5: a) Comparison of the extracted mean value μ_p of protons (diamond) for the individual Gaussian and the total fit (star) in β-distribution as a function of the momentum in the RPC. The theoretical β proton values are given by the black line. b) Extracted resolution σ_p of the protons (diamond) for the individual Gaussian and the total fit (star) together with the second-order polynomial fit shown by the solid magenta curve.

To make sure that the graphical cut selects nearly all protons while excluding most other particle species, the graphical cut was constructed with 2σ around the mean μ_p. Figure 4.6 displays the resulting graphical selection based on the β and momentum p correlation separately for RPC (Fig. 4.6 a)) and TOF (Fig. 4.6 b)). The selected momentum range for the graphical cut is in between 360 MeV/c and 1600 MeV/c for RPC and in between 300 MeV/c and 1100 MeV/c for TOF. The same procedure, as discussed before, was also applied to the GiBUU simulation to extract the same graphical selection. The same selection range was used as well.

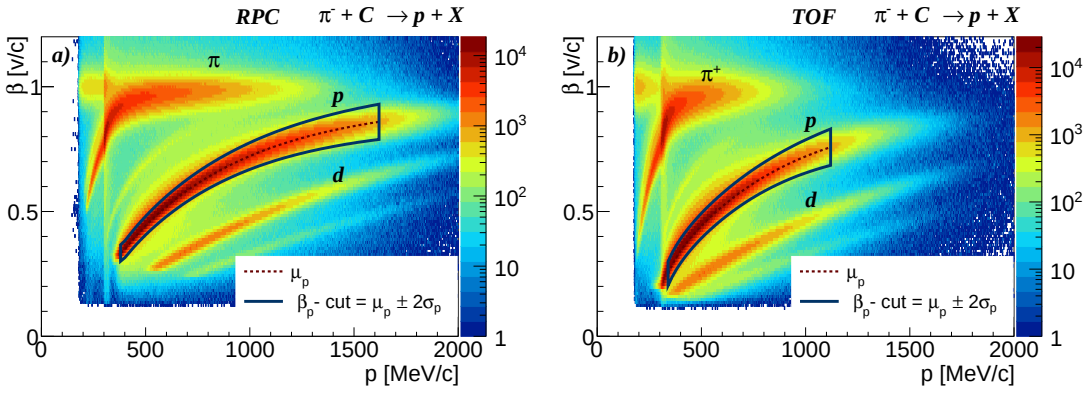

Figure 4.6: $p - \beta$ distribution for positive charged particles in $\pi^- + \mathrm{C}$ collisions together with the $\pm 2\sigma_p$ graphical cut (dark blue solid curve) for protons around μ_p (red dashed curve) for RPC (a)) and TOF (b)).

To quantify the proton purity after the graphical selection, experimental and simulated mass distribution of the protons in different p_t-y ranges were investigated. In the following it has not been distinguished between RPC and TOF. In order to compare the experimental and the simulated mass spectra each simulated mass distribution was scaled by the following factor (Eq. 4.1.5) where $m_{p,\,min} = 800\,\mathrm{MeV/c^2}$, $m_{p,\,max} = 1200\,\mathrm{MeV/c^2}$ denote the minimal and the maximal calculated proton masses

$$SF = \frac{\int_{m_{p,\,min}}^{m_{p,\,max}} m_{p,\,\mathrm{Exp}}}{\int_{m_{p,\,min}}^{m_{p,\,max}} m_{p,\,\mathrm{GiBUU\ PID\ 14}}}. \tag{4.1.5}$$

$m_{p,\,\mathrm{Exp}}$ represents the experimental proton mass distribution and $m_{p,\,\mathrm{GiBUU\ PID\ 14}}$ represents the simulated proton mass distribution with the GEANT PID information to verify that only real protons are selected. Figure 4.7 compares the experimental and simulated mass distributions. One can see that the scaled simulated mass distribution after the graphical selection (blue curve) as well as the additional GEANT PID information (filled area) reproduces the experimental spectrum (black points) well.

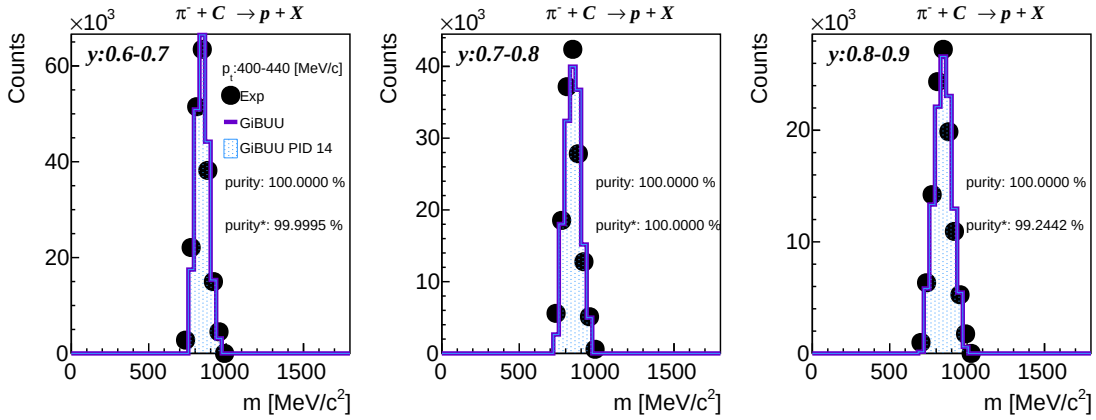

Figure 4.7: Comparison of the mass distribution in $\pi^- + \mathrm{C}$ reactions for the experimental data (black points) and the simulation with (filled area) and without (blue curve) GEANT PID information. The shown transverse momentum range lies between $400 - 440\,\mathrm{MeV/c}$ with varying rapidity ranges from 0.3 to 0.7.

As the mass resolution in experiment and simulation are in good agreement, one can not only extract the purity (purity) in the simulated data by comparing the proton yield of the integrated mass spectra with and without GEANT PID information (Eq. 4.1.6), but also the experimental purity (purity*) (Eq. 4.1.7).

$$purity = 100 \cdot \left| 1 - \frac{N(m_{\mathrm{GiBUU}}) - N(m_{\mathrm{GiBUU\ PID\ 14}})}{N(m_{\mathrm{GiBUU\ PID\ 14}})} \right| \tag{4.1.6}$$

In Equation 4.1.6 and Eq. 4.1.7 $N(m_{\text{GiBUU}})$ represents the simulated yield after integrating the mass distribution for each p_t and y bin, while $N(m_{\text{GiBUU PID 14}})$ stands for the simulated yield with GEANT PID information and $N(m_{\text{Exp}})$ for the experimental yield.

$$purity* = 100 \cdot \left| 1 - \frac{N(m_{\text{Exp}}) - N(m_{\text{GiBUU PID 14}})}{N(m_{\text{GiBUU PID 14}})} \right| \tag{4.1.7}$$

In addition, to get a proper comparison and thus a correct purity calculation, there need to be enough entries in the simulation data. In this analysis only bins with more than 300 entries are included.

Figure 4.8 a) depicts the purity distribution which is nearly 100% over the whole phase space and averages at 99.997%. In Figure 4.8 b) the purity* is shown. In both cases, bins with a purity below 60% were excluded.

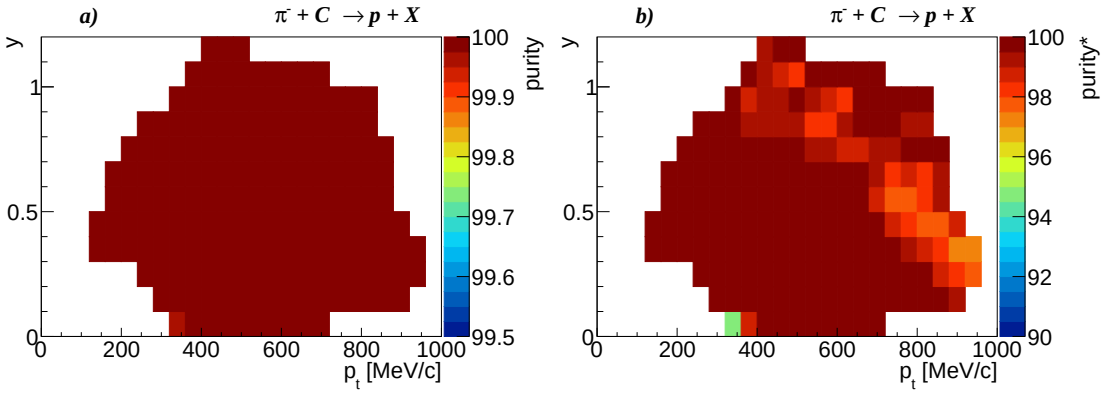

Figure 4.8: Purity of the protons as a function of transverse momentum and rapidity for simulation a) and experimental data b) in π^- + C reactions.

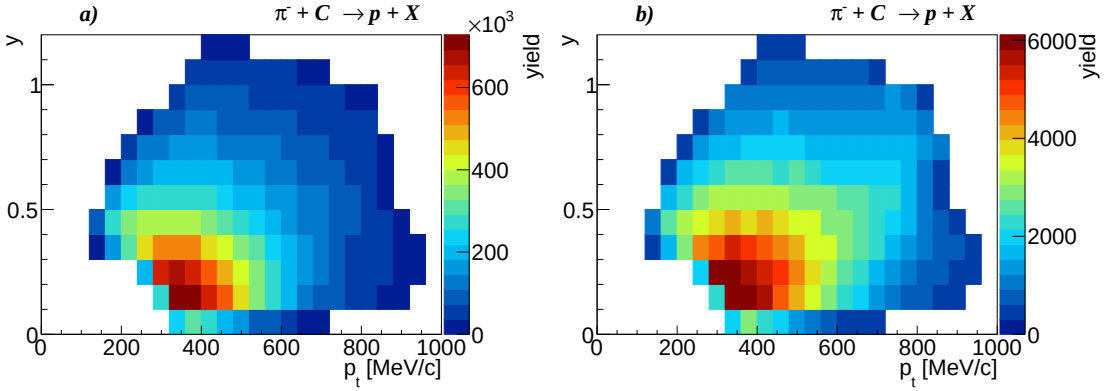

Figure 4.9: Reconstructed yield of p as a function of the transverse momentum and rapidity inside the HADES acceptance in π^- + C collisions for experimental a) and simulated data b).

Figure 4.9 a) depicts the reconstructed proton yield in the experimental data. The proton yield is mainly distributed between $0 < y \leq 1.2$ and $0 < p_t \leq 1000\,\mathrm{MeV/c}$ with a maximum around $p_t = 400\,\mathrm{MeV/c}$ and $y = 0.2$. At lower transverse momenta and rapidity the population decreases until the HADES acceptance is reached. In Figure 4.9 b) the phase space distribution of the extracted yield in GiBUU simulation is shown. Both, the experimental and simulated double-differential distributions look quite similar. The chosen binning for GiBUU simulation and experiment is the same all over this analysis.

4.1.3 Acceptance and Efficiency Correction

As discussed in Chapter 2, the measurement is limited by the geometrical HADES acceptance. Besides, the detector response or the final analysis procedure including for example the particle identification and the applied cuts introduce inefficiencies.

The corrections for these effects are performed with the help of full-scale simulations e.g. based on transport model calculations (Section 3.1). The complete chain of simulation tools is described in detail in Section 3.2. It consists of an event generator, in this case GiBUU, in which the initial conditions like employed target and beam particles are set. Event generators cover the full available phase space of the studied reaction while the influence of the detector which contains particle interaction with the detector material, scattering and energy loss, are treated in the HGeant framework. The efficiency effects caused by the detector response are taken into account in the SimDST production.

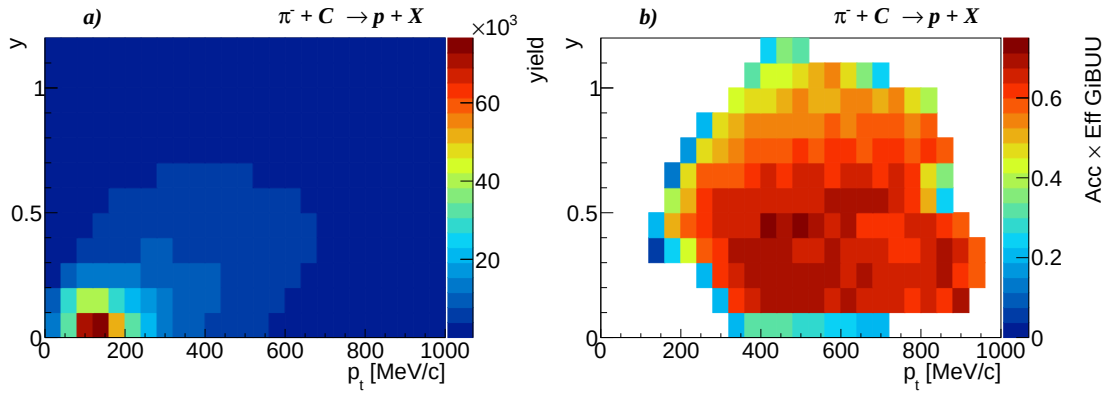

Figure 4.10: a) Initial full-scale $p_t - y$ distribution for GiBUU in $\pi^- + \mathrm{C}$ collisions. b) Acc⊗Eff matrix for the GiBUU simulation as a function of transverse momentum and rapidity in $\pi^- + \mathrm{C}$ collisions.

The SimDST output format is similar to the format of the experimental data. As a last step, the simulated data is analysed exactly in the same way as the experimental data. In

this way the full-scale simulation is obtained. This includes finally the losses caused by, for example, the event selection (Section 4.1.1) and the particle identification (Section 4.1.2). This allows to calculate a correction matrix $\epsilon_{corr}(p_t, y)$ for the experimental spectrum according to Eq. 4.1.8 based on the initial $\epsilon_{in}(p_t,y)$ and reconstructed simulation $\epsilon_{final}(p_t,y)$

$$\epsilon_{corr}(p_t, y) = \frac{\epsilon_{final}(p_t,y)}{\epsilon_{in}(p_t,y)}. \tag{4.1.8}$$

The initial simulated distribution in the double-dimensional $p_t - y$ distribution in π^- + C reactions which is not limited by the geometrical HADES detector acceptance is represented in Fig. 4.10 a). Most of the protons are populated in the range $p_t < 200\,\mathrm{MeV/c}$ and $y < 0.1$. But they dont't fly inside the acceptance of the HADES detector. The acceptance and efficiency correction matrix (Fig. 4.10 b)) is obtained by dividing the initial GiBUU phase space distribution of protons by the reconstructed spectrum. The average acceptance and efficiency is around 55.67%.

At the edges of the detector acceptance the combined acceptance and efficiency drops down to 10%. Finally, by dividing the measured yield through the acceptance and efficiency matrix, an unbiased proton spectrum is obtained (Fig. 4.11). The latter can be used for physical interpretations. Fig. 4.11 a) displays the unbiased proton yield for π^- + C reactions with a maximum yield population in $200 < p_t < 400\,\mathrm{MeV/c}$ and $0 < y < 0.3$. Going to higher transverse momenta and beam rapidity the proton yield decreases. The number of corrected protons for π^- + C reactions is $N^{\mathrm{C}}_{\mathrm{corr}} = 5.5 \cdot 10^7$ In Figure 4.11 b) the unbiased yield for π^- + W collisions is represented which shows almost the same behaviour with a number of corrected protons $N^{\mathrm{W}}_{\mathrm{corr}} = 1.1 \cdot 10^8$.

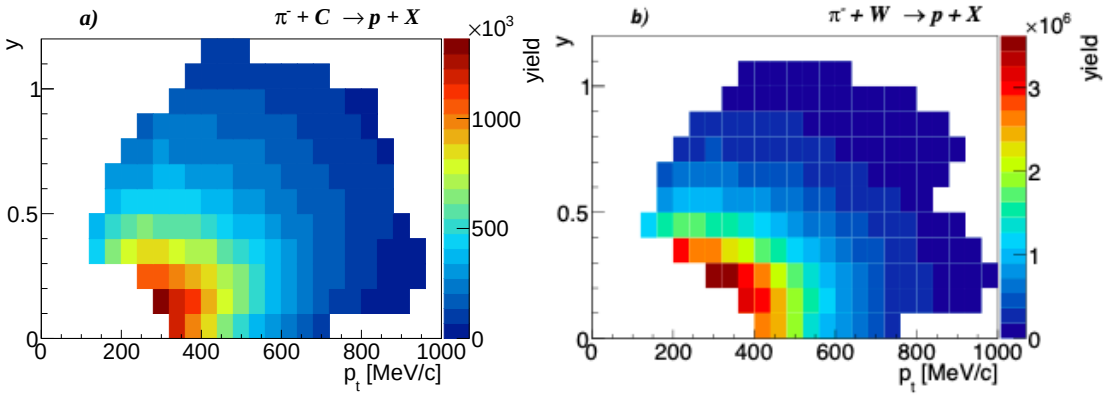

Figure 4.11: Unbiased corrected proton yield as a function of transverse momentrum p_t and rapidity y in π^- + C a) and π^- + W b) reactions.

A precise method to validate the applied correction is a self-consistency check. To archive this, a second transport model, in this case UrQMD was used. The unfiltered double-differential spectrum based on UrQMD is presented in Fig. 4.12 a). After processing the UrQMD data through the same full scale analysis as discussed in Chapter 3, the acceptance and efficiency matrix was obtained and applied to the experimental data (Fig. 4.12 b)).

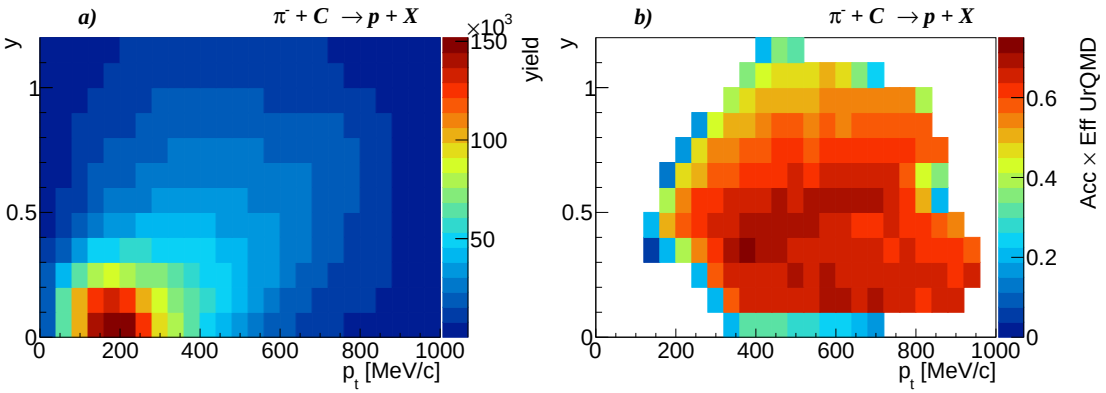

Figure 4.12: a) Initial full-scale $p_t - y$ distribution for UrQMD in $\pi^- + \mathrm{C}$ reactions. b) Acc⊗Eff matrix for the UrQMD transport model as a function of transverese momentum and rapidity in $\pi^- + C$ collisions.

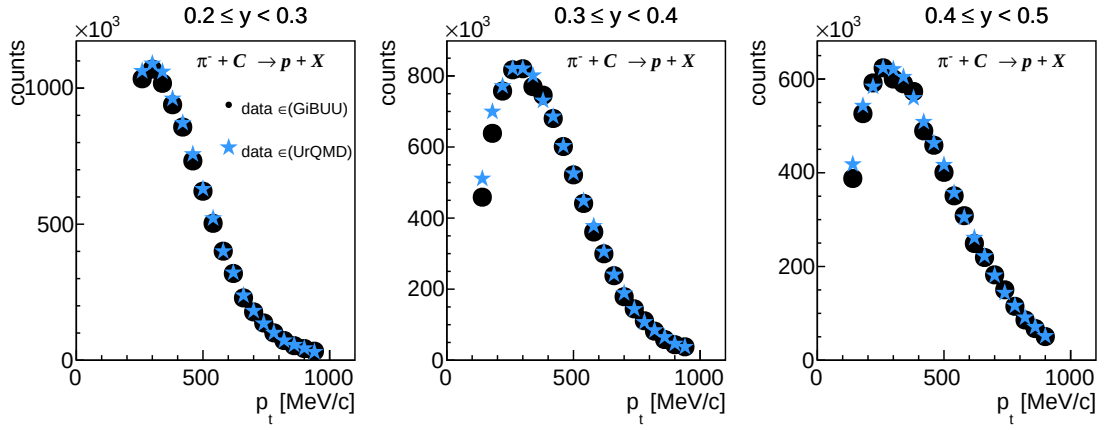

Figure 4.13: Corrected experimental p_t spectrum in $\pi^- + \mathrm{C}$ reactions for rapidity regions ranging form $y = 0.2 - 0.5$ based on GiBUU (black points) and UrQMD (blue stars) correction matrices.

To confirm the model independence of the applied method, the resulting acceptance and efficiency corrected p_t distributions, based on GiBUU and UrQMD, were projected on the rapidity axis and compared to each other. The comparison is shown in Fig. 4.13 for three different rapidity regions. For both models the corrected experimental p_t spectra

are in good agreement. At the HADES detector acceptance border minor differences are visible, which can be attributed to statistical fluctuations. The comparison confirms the assumption that the correction in these two kinematic independent variables is not related to the underlying model. In the subsequent analysis the GiBUU corrected spectrum was applied.

4.1.4 Systematic and Statistical Uncertainties

The statistical error of the double-differential proton distribution is nearly negligible due to the high collected statistics. As shown in the $\beta-$distribution in Fig. 4.4, the proton peak is isolated with almost no background which is also resembled by the high purity (Fig. 4.8). Therefore, the statistical error calculation is simplified to (Eq. 4.1.9)

$$\Delta N_{stat} = \frac{1}{\sqrt{N_{\text{uncorr}}}} \cdot N_{\text{corr}}. \tag{4.1.9}$$

N_{uncorr} denotes the number of uncorrected protons while N_{corr} is the number of corrected protons. The relative statistic error $\Delta N_{\text{stat, rel}} = \frac{1}{\sqrt{N_{\text{uncorr}}}}$ is about 0.002% for Carbon and about 0.01% for Tungsten.

Systematic uncertainties come along with every experimental measurement. In the present analysis a 2σ selection around the expected value for protons in the $\beta - p$ distribution is applied to select a high proton purity sample. To discover any significant influence introduced by the proton identification, the analysis was repeated for 1.5σ and 2.5σ graphical selection (Fig. 4.14). In Figure 4.15 the variation of the corrected experimental yield as a function of p_t due to the proton identification are compared to each other. One can see that there are no significant variations (ΔN_{var}) and hence these corresponding uncertainties are small. However, the difference was considered in the systematic error evaluation in the following way (Eq. 4.1.10) where $N_{\text{max, corr}}$ and $N_{\text{min, corr}}$ represent the maximum and minimum corrected yield.

$$\Delta N_{\pm,\text{ var}} = \frac{|N_{\text{max/min,corr}} - N_{\text{corr}}|}{N_{\text{corr}}}, \tag{4.1.10}$$

The variation error ΔN_{var} is nearly negligible as it is on average far below 1%. Besides, the efficiency error ΔN_{eff} of 3% [18] due to the detector response was taken into account in the systematic uncertainties. So the systematic error is dominated by the efficiency error ΔN_{eff}. According to Eq. 4.1.11 the systematic error on the obtained yield of protons is then in the order of 3% when summing up quadratically the variation of the β-cut

(ΔN_{var}) and the efficiency correction (ΔN_{eff})

$$\Delta N_{\pm,\text{sys}} = \sqrt{\Delta N^2_{\pm,\text{var}} + \Delta N^2_{\text{eff}}} \approx 3\%. \tag{4.1.11}$$

For the rapidity density distribution ΔN_{extra} was considered in the systematic error calculation. ΔN_{extra} arises from the extrapolation to unmeasured transverse p_t regions and will be explained in Section 4.1.5. For the rapidity density distribution the total systematic error amounts to

$$\Delta N_{\pm,\text{sys}} = \sqrt{\Delta N^2_{\pm,\text{var}} + \Delta N^2_{\text{eff}} + \Delta N^2_{\text{extra}}} \approx 15\% \tag{4.1.12}$$

where ΔN_{extra} is the error of the Boltzmann extrapolation (Section 4.1.5) to unmeasured p_t regions and which is on average about 15%.

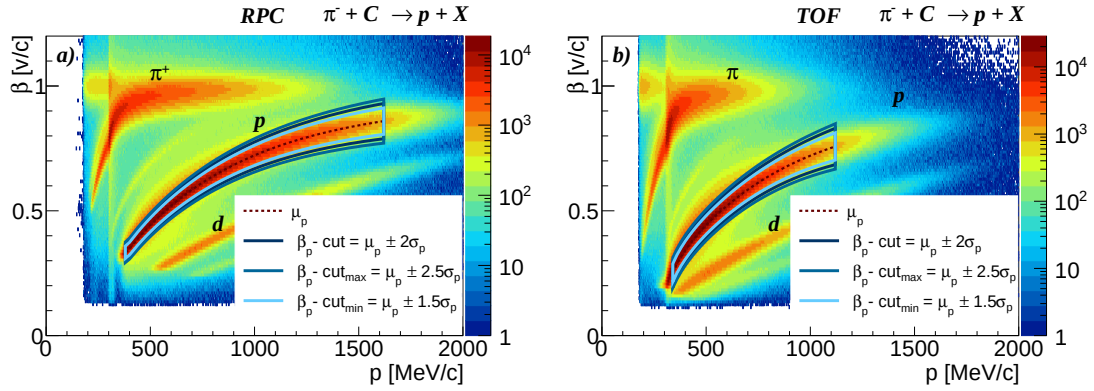

Figure 4.14: $p - \beta$ spectrum in $\pi^- + \text{C}$ reaction separated for RPC a) and TOF b). The 1.5σ, 2σ and 2.5σ selection around μ_p (red dashed curve) indicated by the light blue, mid blue and dark blue curve, respectively.

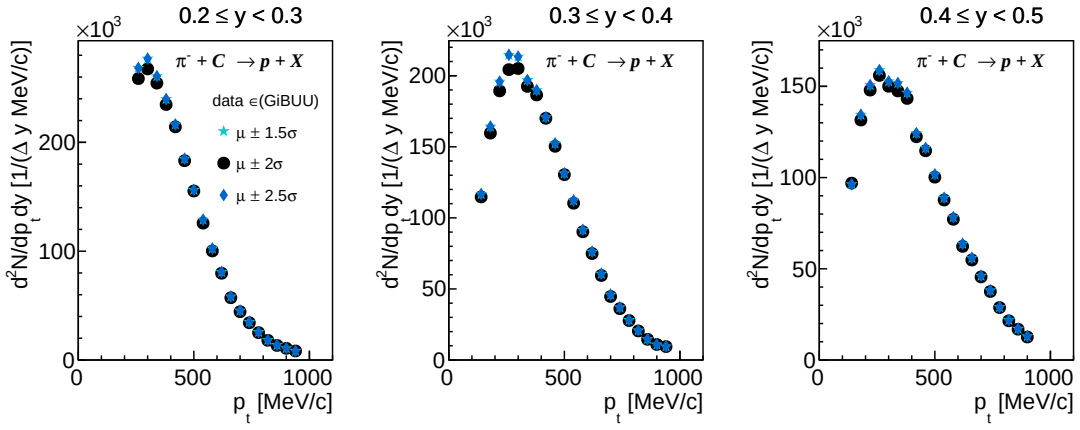

Figure 4.15: Double-differential p_t distribution in $\pi^- + \text{C}$ reactions for rapidity regions ranging from $y = 0.2 - 0.5$ with the graphical selection for 1.5σ (light blue stars), 2σ (black points) and 2.5σ (blue diamonds).

4.1.5 Transverse Momentum Extrapolation

Another important quantity is the rapidity density distribution $\frac{dN}{dy}$ (Fig.4.17 b)). It is obtained by the integration of the two-dimensional phase space over p_t. Inside the HADES acceptance the unmeasured p_t regions are dependent on the selected rapidity range. One can see in Fig. 4.16 that the acceptance is limited at very low and very high transverse momenta (in average $p_t < 300\,\mathrm{MeV/c}$ and $p_t \geq 900\,\mathrm{MeV/c}$). To also extract the yield in the unmeasured regions, a Boltzmann fit (Eq. 4.1.13) can be used. This approach has been employed for various collision systems [17] [20]. It is especially used in heavy-ion collisions [17]. Even though, studies from [26] show that the Fermi motion forces the p_t spectra to follow a Boltzmann shape. Thus, a Boltzmann fit was applied to the experimental data allowing to extrapolate the yield in the low and high p_t range which is not covered by HADES. In Equation 4.1.13 $A(y)$ denotes the amplitude, m_p the proton mass and $T_B(y)$ stands for the inverse slope parameter

$$\frac{dN}{dp_t dy} = A(y) \cdot p_t \cdot \sqrt{p_t^2 + m_p^2} \cdot e^{-\frac{\sqrt{p_t^2 + m_p^2}}{T_B(y)}}. \tag{4.1.13}$$

Both, the amplitude and the inverse slope parameter are rapidity dependent free fit parameters.

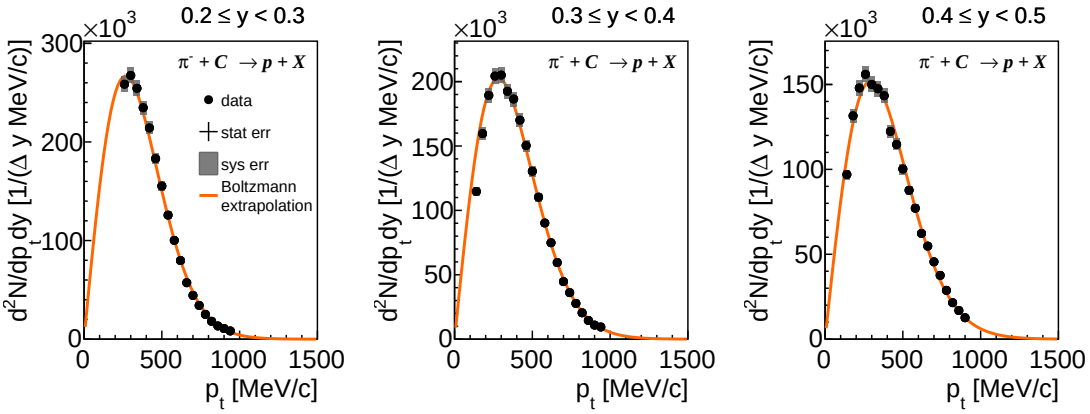

Figure 4.16: Double-differential distribution as a function of p_t in $\pi^- + \mathrm{C}$ reactions for certain rapidity regions $y = 0.2 - 0.5$. The Boltzmann extrapolation is indicated by the orange curve. The statistic and systematic uncertainties are given by error bars and grey boxes, respectively.

The corrected p_t-spectrum for a rapidity range of $0.2 \leq y < 0.5$, including the statistical and systematic errors is shown in Fig. 4.16. Also, the Boltzmann fit, is sketched in Fig. 4.16. As demonstrated in Fig 4.16, the Boltzmann fits (orange curve) are in rather good

agreement with the experimental data over the entire rapidity range.

The rapidity dependent inverse slope parameter was extracted from the Boltzmann fit and is pictured in Fig. 4.17 a). In this plot, the values are increasing when the rapidity gets larger. Comparing the inverse slope parameter as function of rapidity (4.17 a)) with the double-differential distributions as a function of p_t (4.16), one can see that small T_B values belong to sharp distributions with a maximum at small transvere momenta. With the increasing T_B values the distributions in Fig. 4.16 also gets broader and so the percantage of protons with large transverse momenta has a has a bigger contribution.

The total yield $\left(\frac{dN}{dy}\right)$ as a function of rapidity in $\pi^- + \mathrm{C}$ collisions is displayed in Fig. 4.17 b) and was obtained on basis of the sum of all measured data points and two integrals at high and low p_t range extrapolated with the Boltzmann fit (Eq. 4.1.14).The data points in the rapidity range ($0.0 < y < 1.0$) are shown including their statistical errors (error bars) and systematic errors (gray boxes). The statistical uncertainties are smaller than the marker points.

$$\frac{dN}{dy} = \int_0^{\mathrm{Nstart}} \frac{dN}{dp_t dy} dp_t + \sum N_{\mathrm{corr}} \cdot \Delta p_t + \int_{\mathrm{Nstop}}^{1500\,MeV/c} \frac{dN}{dp_t dy} dp_t. \tag{4.1.14}$$

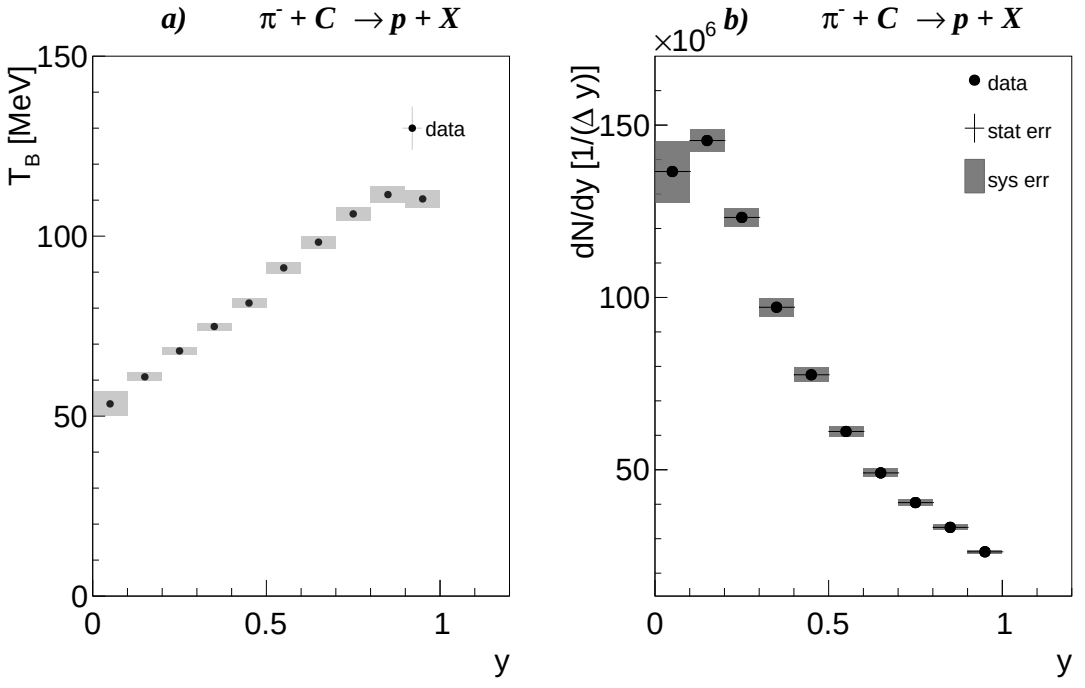

Figure 4.17: a) Inverse slope parameter T_B as a function of rapidity in $\pi^- + \mathrm{C}$ reactions from the Boltzmann fit. b) Total yield as function of rapidity in $\pi^- + \mathrm{C}$ reactions. The statistic and systematic uncertainties are indicated by the error bars and filled areas, respectively.

4.1.6 Absolute Normalization

To obtain the proton production cross-section an absolute normalization is necessary. The cross-section (Eq. 4.1.15) is dependent on the number of reconstructed protons (N), the incident number of pions (N_{beam}) the solid target density ρ, the mass number of the target nucleus A, the Avogadro constant N_A and the target thickness d_{target}

$$\sigma = \frac{N}{N_{\text{beam}} \cdot (\rho/A) \cdot N_A \cdot d_{\text{target}}}. \tag{4.1.15}$$

The number of incident pions ($N_{\text{beam}} = N_{T_0} \cdot (1 - t_{\text{dead}})(0.81 \pm 0.1)$) which reached the target, is calculated based on the number of particles N_{T_0}, which were detected in the target-T_0 detector. The latter has to be corrected with the dead time of the HADES data acquisition system. Moreover, the geometrical acceptance has to be taken into account, as the target-T_0 detector area is bigger than the one of the solid target. The given uncertainty arises from the beam transport simulation. Moreover, another uncertainty (10%) arising from the N_{T_0} variation has to be considered. The individual observables for the cross-section calculation are listed in Table 4.1.

Table 4.1: Summary of relevant physical observables to calculate the absolute normalization.

Target	A	$\rho\,[g/cm^3]$	$d_{\text{target}}\,[cm]$	N_{T_0}	$t_{\text{dead}}\,[\%]$
C	12.011	1.85	0.72	$4.31 \cdot 10^9$	0.156
W	183.84	19.3	0.24	$4.16 \cdot 10^9$	0.154

4.2 Results and Discussion

In the following section the double-differential cross-sections of both, $\pi^- + \mathrm{C}$ and $\pi^- + \mathrm{W}$, collision systems and their integrated differential production cross-sections will be presented.

4.2.1 $P_t - y$ Distribution

The double-differential yield was normalized to the number of beam particles and target thickness as explained in Section 4.1.6. The rapidity dependent differential cross-sections in $\pi^- + \mathrm{C}$ and $\pi^- + \mathrm{W}$ reactions are shown in Fig. 4.18 and Fig. 4.19. The dominant error of the double-differential cross-section (Fig. 4.18 and Fig. 4.19) is the normalization error due to the beam intensity uncertainty which is in average about 15%. Here a Boltzmann fit was applied to extrapolate to the unmeasured p_t regions (Section 4.1.5). The latter is indicated as violet curve in Fig. 4.18 and as orange curve in Fig. 4.19. The Boltzmann fits are in good agreement with the experimental data (dark points) in the rapidity ranges $0 < y < 1$ for $\pi^- + \mathrm{C}$ reaction and $0 < y < 0.9$ for $\pi^- + \mathrm{W}$ collision. At higher rapidity $y > 1.0$ ($\pi^- + \mathrm{C}$) and $y > 0.9$ ($\pi^- + \mathrm{W}$) the p_t coverage of the experiment is not sufficient to constrain the fit.

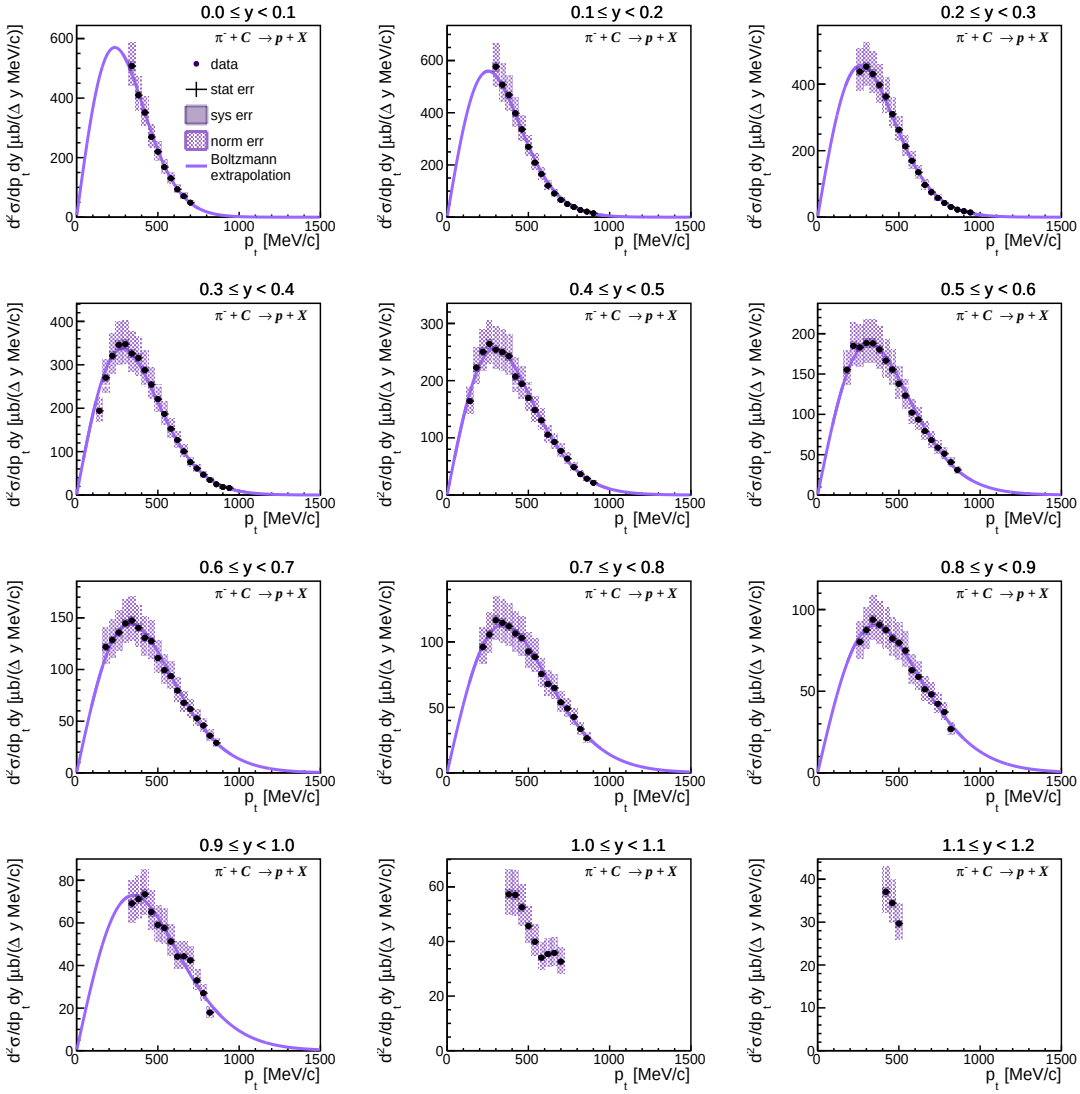

Figure 4.18: Double-differential cross-section in $\pi^- + \mathrm{C}$ reactions for rapidity regions ranging between $0 < y < 1.2$. The Boltzmann fit is indicated by the violet curve. The statistic, systematic and normalization uncertainties are given by error bars, filled and dotted violet boxes.

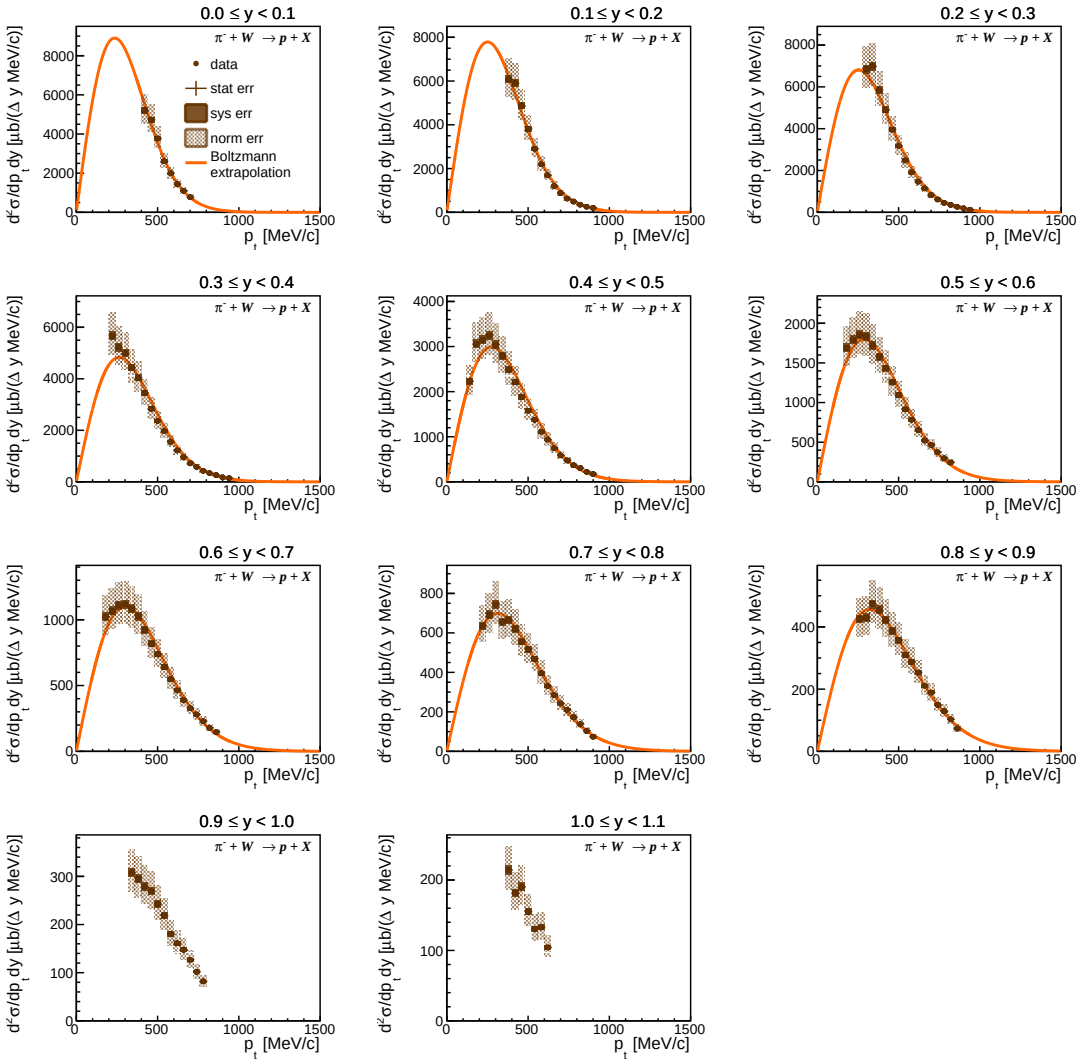

Figure 4.19: Double-differential cross-section in $\pi^- + \mathrm{W}$ reactions for rapidity regions ranging between $0 < y < 1.2$. The Boltzmann extrapolation is indicated by the orange curve. The statistic, systematic and normalization uncertainties are given by error bars, filled and dotted orange boxes.

4.2.2 Rapidity Density Distribution

By summing up all measured data points and the two integrals of the Boltzmann extrapolation in the region not covered by the HADES acceptance, the integrated differential cross-section as a function of the rapidity for both collision systems in the rapidity range $0 < y < 1.0$ ($\pi^- + \mathrm{C}$) and $0 < y < 0.9$ ($\pi^- + \mathrm{W}$) was obtained. The latter are presented in Fig. 4.20. The shape of the rapidity distribution is quite similar for both collision systems. By integrating over the rapidity dependent cross-section the differential production cross-sections ($\Delta\sigma$) in $\pi^- + \mathrm{C}$ ($0 < y < 1.0$) and in $\pi^- + \mathrm{W}$ ($0 < y < 0.9$) was calculated and is listed in Table 4.2.

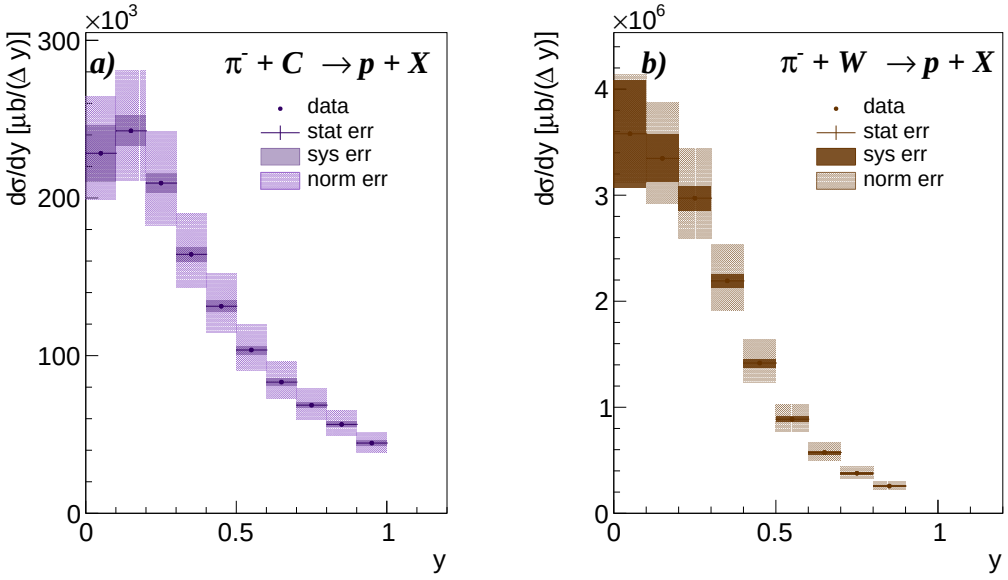

Figure 4.20: Proton production cross-section as a function of rapidity for $\pi^- + \mathrm{C}$ a) and $\pi^- + \mathrm{W}$ b) reactions. The statistical errors (error bars) are smaller than the symbol size. The systematic uncertainties are indicated by filled boxes, while the normalization errors are displayed as dotted boxes.

Table 4.2: Target and integrated differential cross-section for protons in $\pi^- + \mathrm{C}$ ($0 < y < 1.0$) and $\pi^- + \mathrm{W}$ ($0 < y < 0.9$) reactions. The absolute error values are given in the following order: statistic (first), systematic (second) and normalization (third).

Target	$\Delta\sigma$ [μb]
C	$133127 \pm 3 \pm 20569^{+20918}_{-17115}$
W	$1560370 \pm 192 \pm 563353^{+245188}_{-200609}$

4.3 Comparison to Transport Model Calculation and HARP Data

After calculating the total production cross-sections in $\pi^- + \mathrm{C}$ and $\pi^- + \mathrm{W}$ collisions a comparison to two state-of-the-art hadronic transport models, GiBUU [9] and UrQMD [3], will be presented. Moreover, a comparison with the double-differential proton production cross-sections of the HARP data is provided.

4.3.1 Comparison to GiBUU and UrQMD

The particle production mechanism implemented in these two models was explained in Section 3.1. Both models are based on the BUU equation (Eq. 3.1.1 in Section 3.1). While GiBUU mediates hadron production channels via cross-section parametrization and therefore does not explicitly produce and propagate intermediated resonances, UrQMD is a resonance based model in the low energy regime. Hence, the particle production occurs through two body decay of intermediated resonances.

In the following comparisons in Fig. 4.21 ($\pi^- + \mathrm{C}$) and in Fig. 4.22 ($\pi^- + \mathrm{W}$) the violet (brown) solid line represents the GiBUU model prediction, while the dashed violet (brown) line stands for the UrQMD model prediction.

In Figure 4.21 ($\pi^- + \mathrm{C}$) GiBUU and UrQMD overestimate the data points nearly in all rapidity ranges. The shape of both models are rather comparable over almost the entire rapidity range. The deviation between data points and model predictions decreases with increasing rapidity. For low rapidity ($y < 0.3$), the experimental shape is reproduced very well by both models. In this rapidity region the low transverse momenta regions have no measured data points due to the HADES acceptance. Looking at the unmeasured transverse momenta for the rapidity range $0 < y < 0.3$, the Boltzmann extrapolation does not match to the shape of the transport models. So it could also be possible that in this region a wrong prediction is caused due to the Boltzmann extrapolation. Going to more forward rapidity ($y > 0.2$) the data points are spread out in a wider transverse momentum range. In this rapidity range ($0.2 < y < 0.5$) both models are in good agreement with the experimental data. But also both models change the shape and at high transverse momenta ($p_t > 600\,\mathrm{MeV/c}$) a shoulder, which transforms at higher rapidity to a second peak, is observed. Such peak is not seen in the experimental data. In the target rapidity range ($0 < y < 0.2$) the GiBUU peak is much higher than the peak for UrQMD.

In Figure 4.22 ($\pi^- + \mathrm{W}$) the comparison to transport model calculation shows the same behavior as in Fig. 4.21 ($\pi^- + \mathrm{C}$). The major difference for the heavier target is that the peak prediction for UrQMD in the low rapidity range ($0 < y < 0.2$) is much higher. Also,

the arise of the shoulder appears at higher rapidity. However, the shoulder turning into a second peak is less distinct. In the rapidity regions $0.5 < y < 0.7$ the transport models reproduce the experimental data rather well.

The deviation of both models with the experimental data could be caused by three body final state effects. Three body final states can be produced by intermediated resonances, which decay in the second step. In the current version of UrQMD however three body reactions are not implemented.

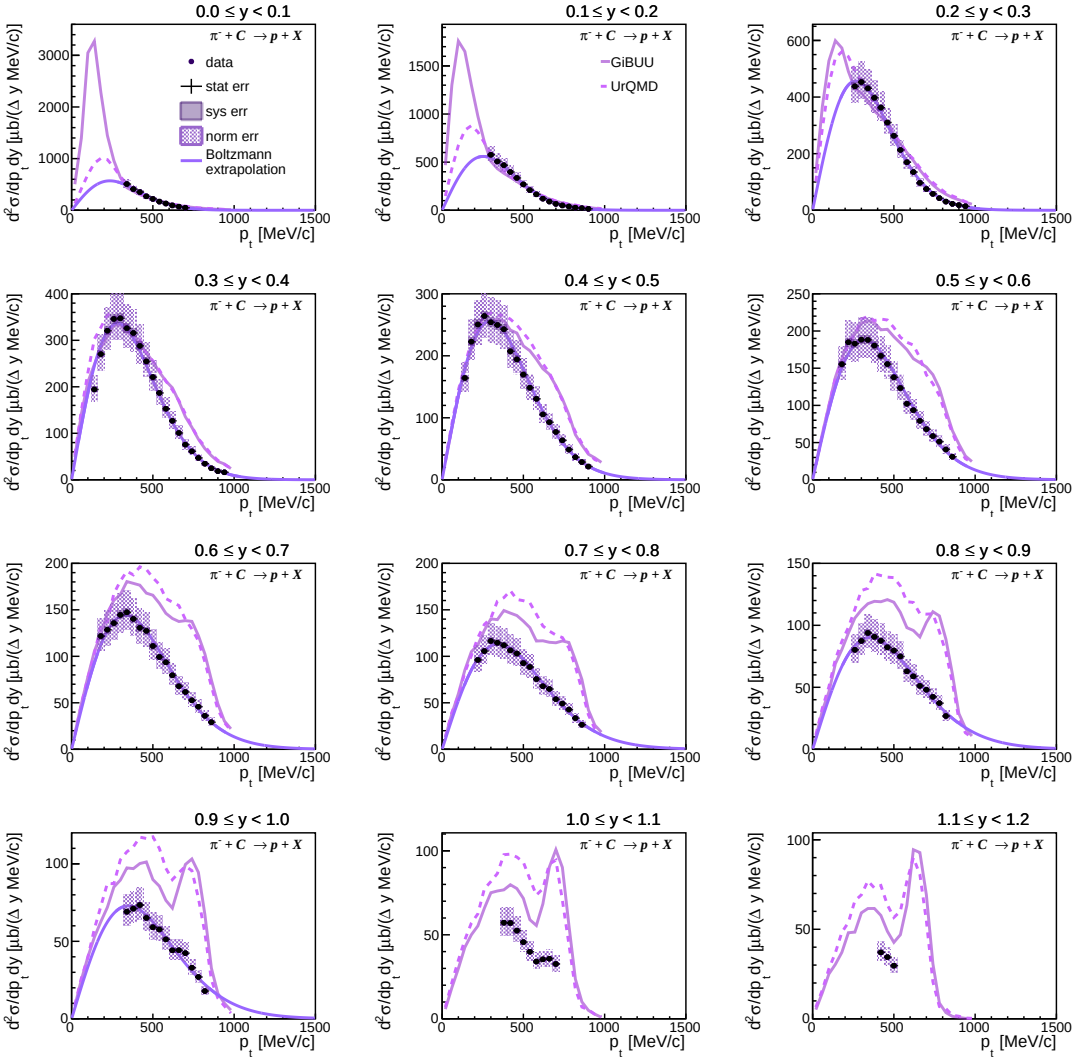

Figure 4.21: Comparison of the double-differential cross-section in $\pi^- + \mathrm{C}$ reaction for rapidity regions $0 < y < 1.2$ to the GiBUU and UrQMD transport models. The Boltzmann fit is indicated by the violet solid line. The statistic, systematic and normalization uncertainties are given by error bars, filled and dotted violet boxes. The GiBUU and UrQMD predictions are given by the solid pink curve and by the dashed pink curve.

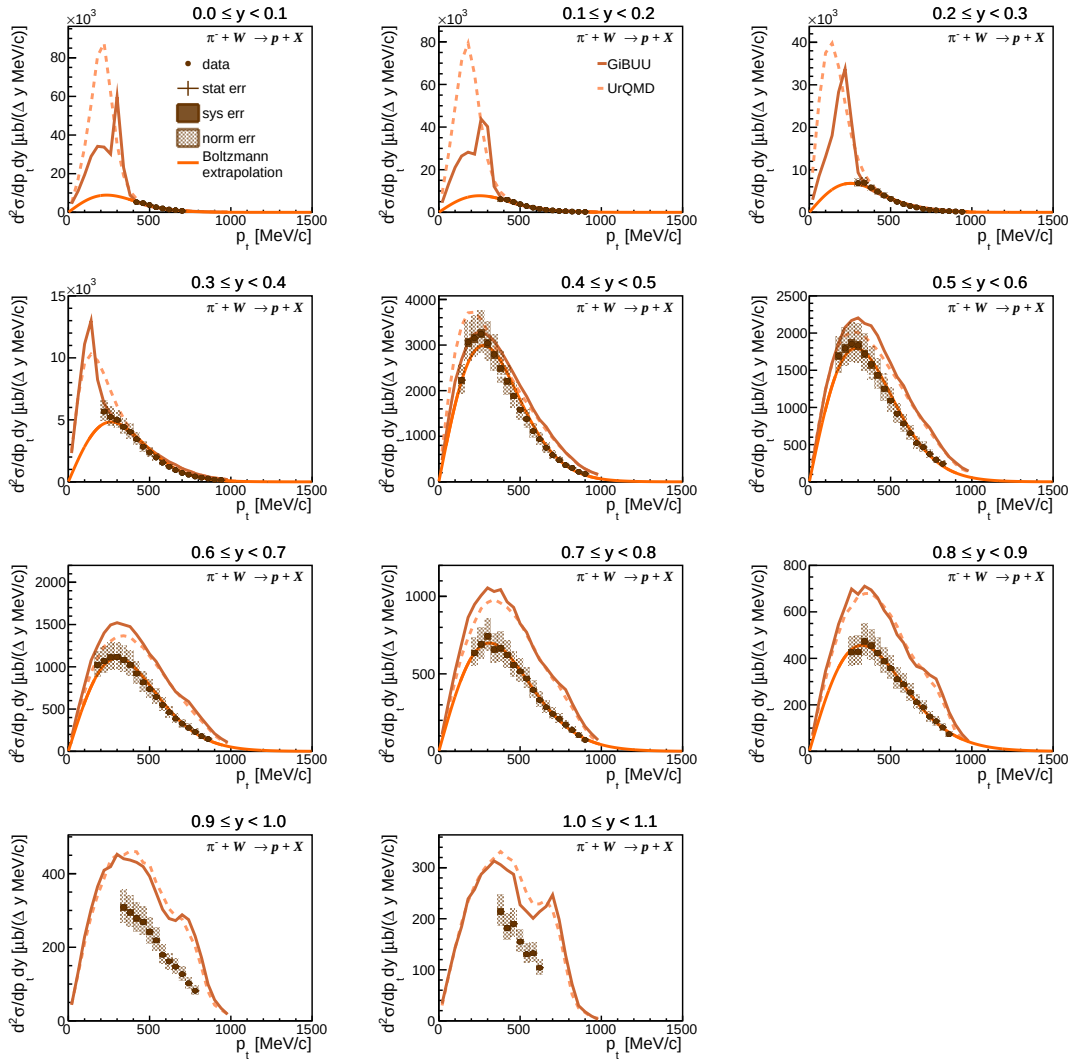

Figure 4.22: Comparison of the double-differential cross-section in $\pi^- + \mathrm{W}$ reaction for rapidity regions $0 < y < 1.2$ the GiBUU and UrQMD transport models. The Boltzmann fit is indicated by the a orange solid line. The statistic, systematic and normalization uncertainties are given by error bars, filled and dotted orange boxes. The GiBUU and UrQMD predictions are given by the solid brown curve and by the dashed brown curve.

The experimental proton production cross-sections in $\pi^- + \mathrm{C}$ and $\pi^- + \mathrm{W}$ reactions, as a function of rapidity (Fig. 4.23), are also compared to the GiBUU and UrQMD transport model predictions. As mentioned before the shape of the two models looks qualitatively similar. The rapidity range for both simulations is in between $-0.5 < y < 1.5$. Both models have in principle the same shape as the experimental data. In the low rapidity region ($0 < y < 0.2$) there is a huge deviation between both models and the experimental data. But looking at Fig. 4.21 and Fig. 4.22 one can see in the low rapidity range

($0 < y < 0.3$), that $p_t < 400\,\mathrm{MeV/c}$ is not measured. The Boltzmann extrapolation in this region does not match the shape of the transport models.

In Figure 4.23 a) where the proton cross-section of $\pi^- + \mathrm{C}$ reaction is shown, the UrQMD model reproduces the experimental data better than the GiBUU model. The shape of both models follows a similar behaviour as the experimental data. However, the peak of both models is shifted to lower rapidity than the experimental peak.

For $\pi^- + \mathrm{W}$ reactions (Fig. 4.23 b)) the peak of the UrQMD prediction close to target rapidity is higher than the GiBUU prediction. For the light carbon target the behaviour was the other way round. Moreover, in Fig. 4.23 b) the shape for both model predictions and the experimental data is nearly the same.

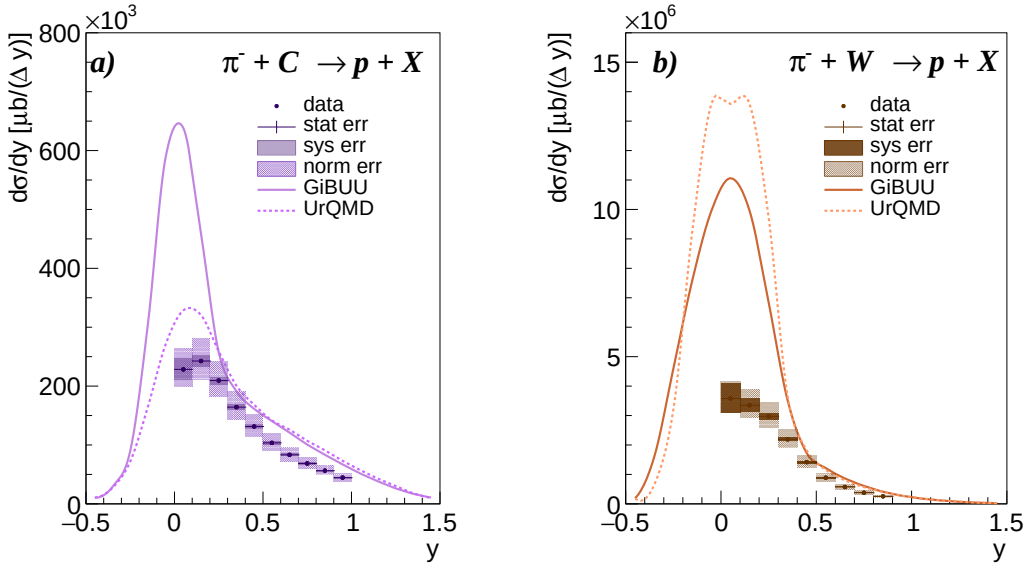

Figure 4.23: Comparison of the experimental proton production cross-section as a function of rapidity to GiBUU (solid curve) and UrQMD (dashed curve) in $\pi^- + \mathrm{C}$ a) and $\pi^- + \mathrm{W}$ b) reactions. Statistical errors which are indicated by error bars are smaller than the marker sizes. The systematic and normalization uncertainties are displayed as filled and dotted boxes, respectively.

4.3.2 Comparison to HARP Data

The same analysis procedure as explained for $p_t - y$ phase space (Section 4.1) was also applied to a second set of independent variables $(p_t, -\theta)$. This second analysis reviews the transverse momentum, ranging from 0 GeV/c − 1 GeV/c and the polar angle in between 10° and 90°. The chosen binning for the transverse momentum p_t is $\Delta p_t = 0.04$ GeV/c and for the polar angel it is $\Delta\theta = 10°$. This second set of independent variables was necessary to compare the experimental double-differential proton cross-sections to the double-differential cross-sections of the HARP Collaboration.

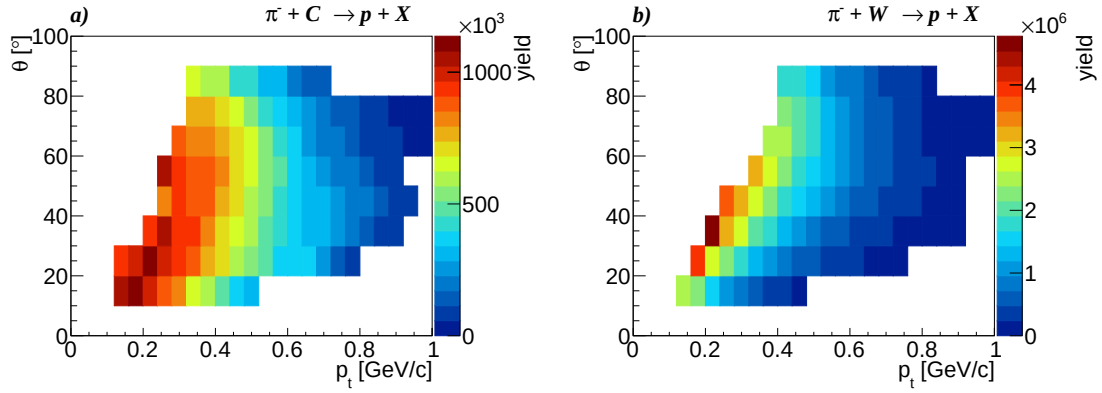

Figure 4.24: Unbiased corrected yield as a function of transverse momentum p_t and polar angle θ in $\pi^- + \mathrm{C}$ a) and $\pi^- + \mathrm{W}$ b) reactions.

The HARP Collaboration performed a systematic measurement of inclusive double-differential cross-sections of hadron production by impinging protons and charged pions with momenta 3, 5, 8, 12, 15 GeV/c with different nuclei (Be, C, Cu, Sn, Ta, Pb) [8]. In Figure 4.25 a comparison of the double-differential cross-section for different polar angle regions in $\pi^- + \mathrm{C}$ reaction at two different incoming beam momenta (HADES: 1.7 GeV/c, HARP [5]: 3 GeV/c) is given. The chosen binning differs at large angles ($\theta > 60°$) and is not included in this comparison. The HADES data are in average in good agreement with the HARP data over the full rage. Figure 4.26 shows the comparison of the double-differential cross-section for the polar angel region ($30° \leq \theta < 40°$) for $\pi^- + \mathrm{C}$ reaction at six different incoming beam momenta ((HADES: 1.7 GeV/c, HARP [5]: 3 GeV/c), 5 GeV/c, 8 GeV/c, 12 GeV/c and 15 GeV/c). For low transverse momenta there is a weak beam dependency. But going to higher transverse momenta this weak dependency depicts until it completely disappears at around $p_t \approx 0.7$ GeV/C.

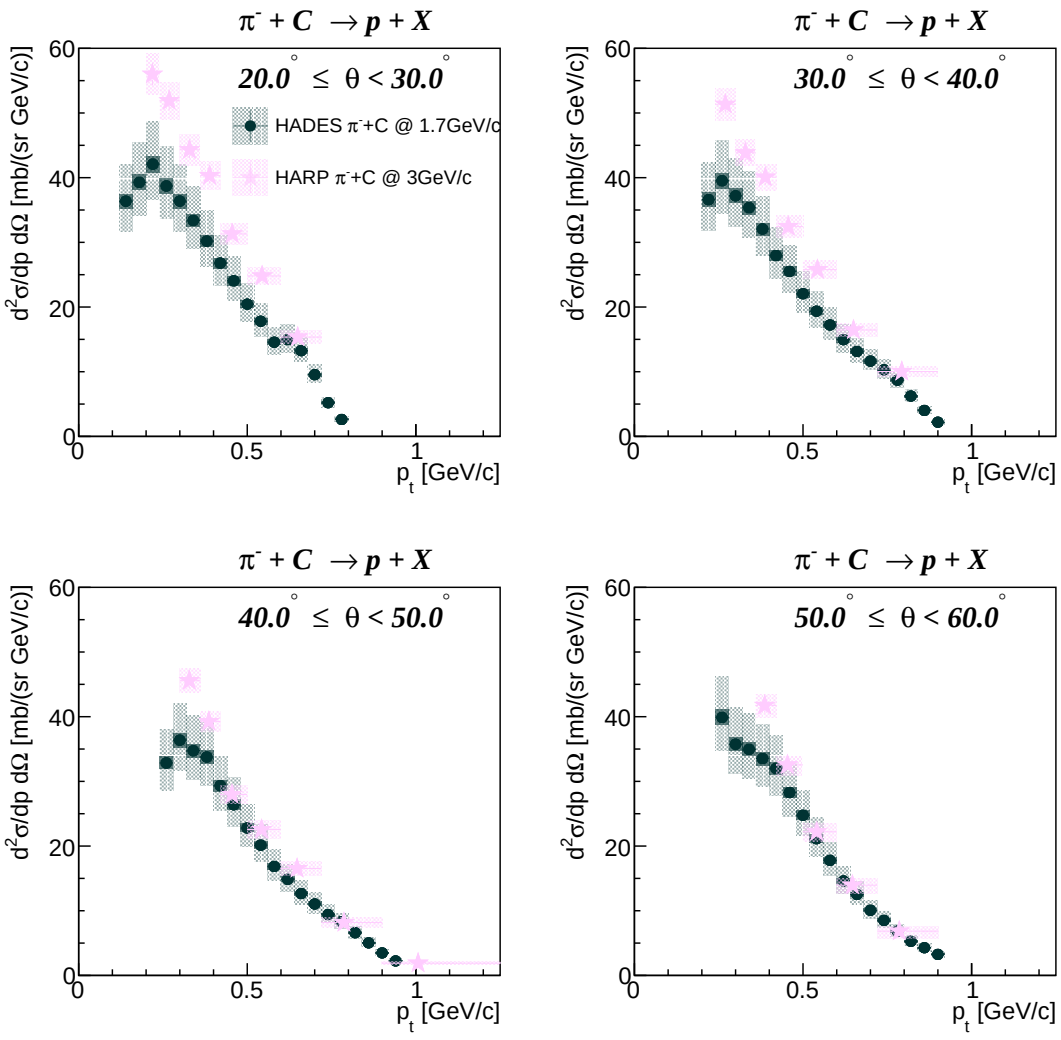

Figure 4.25: Comparison of the double-differential cross-section in $\pi^- + \mathrm{C}$ reaction for polar angle regions $20° < \theta < 60°$ with the HARP data [5] at 3 GeV/c (stars). The statistic, systematic and normalization uncertainties of this work (HADES) are given by error bars, filled and dotted green boxes, respectively.

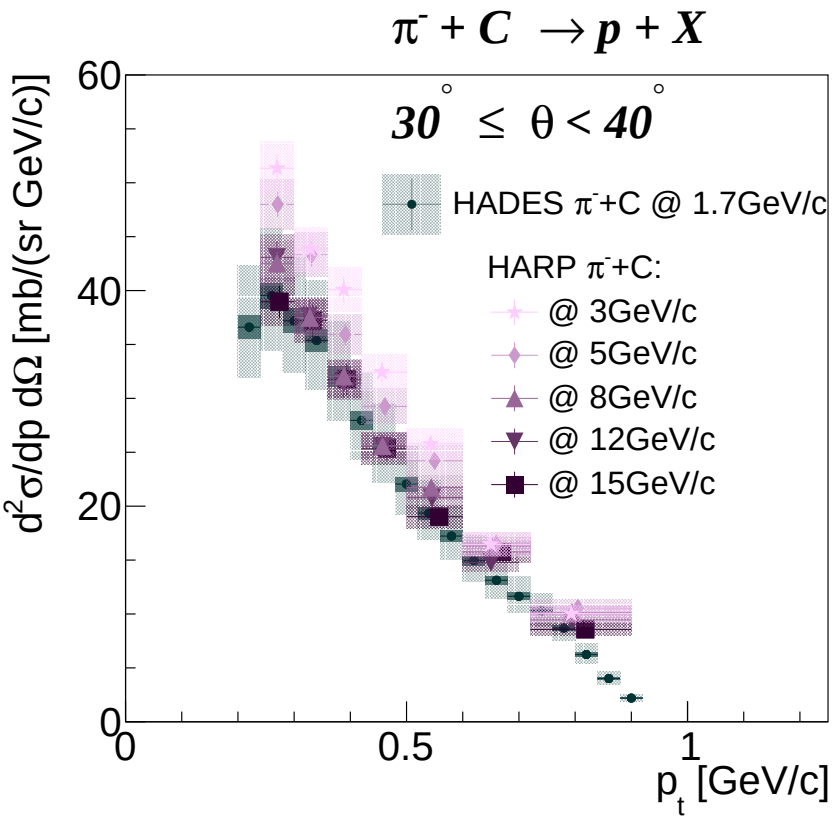

Figure 4.26: Comparison of the double-differential cross-section in $\pi^- + \mathrm{C}$ reaction for polar angle region $30° < \theta < 40°$ with the HARP data [5] with beam momentum 3 GeV/c (stars), 5 GeV/c (diamonds), 8 GeV/c (triangles), 12 GeV/c (mirrored triangles) and 15 GeV/c (boxes). The statistic, systematic and normalization uncertainties of this work (HADES) are given by error bars, filled and dotted green boxes, respectively.

Besides, the weak beam momentum dependency one can also investigate the proton production on the atomic mass number A. In Figure 4.27 the double-differential proton production cross-section in $\pi^- + \mathrm{W}$ reaction at 1.7 GeV/c is compared to the proton production cross-section in $\pi^- + \mathrm{C}$ and $\pi^- + \mathrm{Ta}$ at 3 GeV/c measured by HARP in [5] [6] [7]. One can see, that at lower transverse momenta the atomic mass number A dependency is more distinct than for higher p_t. Reaching $p_t = 1$ GeV/c there is almost no dependency on the atomic number A anymore. The atomic numbers of tungsten ($A = 184$) and tantalum ($A = 180$) are comparable. The difference between them arises from the incoming beam momentum dependency (Fig. 4.28). In Figure 4.28 the comparison of $\pi^- + \mathrm{W}$ at 1.7 GeV/c (HADES) to various incoming beam momenta (3, 5, 8, 12, 15 GeV/c) for $\pi^- + \mathrm{Ta}$ reaction (HARP) is presented, to demonstrate its more distinct behavior for heavier targets than carbon. The incoming beam momentum

dependency for the HARP data in $\pi^- + \mathrm{Ta}$ is distinct for 3 GeV/c and 5 GeV/c. With this, the difference to the smaller values for the measured data in $\pi^- + \mathrm{W}$ at a lower incoming beam momentum (1.7 GeV/c) can be explained. Reaching higher incoming beam momenta this dependency disappears. In general, one can see an increase of the proton production cross-section with larger atomic numbers for $p_t < 1\,\mathrm{GeV/c}$.

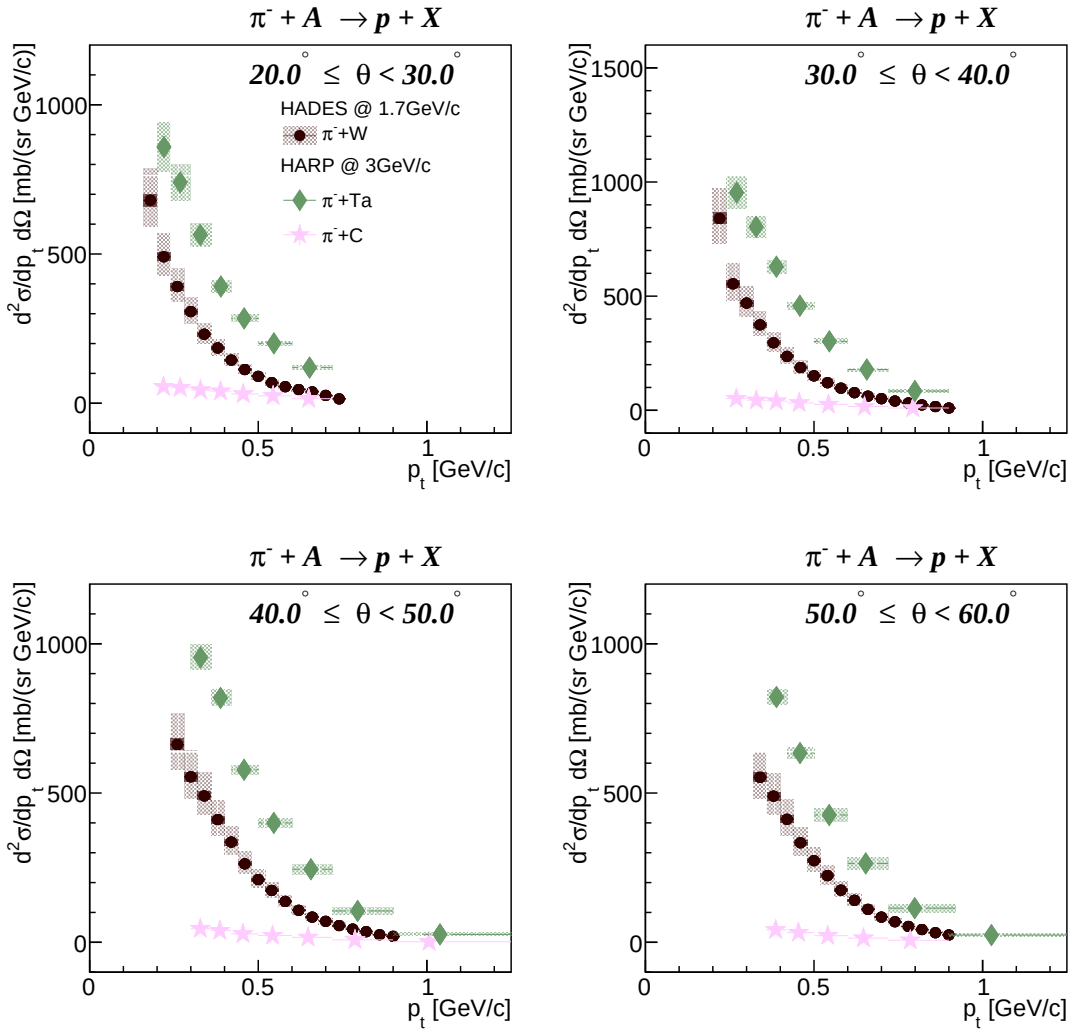

Figure 4.27: Comparison of the double-differential cross-section in $\pi^- + \mathrm{W}$ (brown dots) reaction at 1.7 GeV/c with π^-+C (violet stars) and π^-+Ta (green diamonds) at 3 GeV/c. The statistic, systematic and normalization uncertainties are given by error bars, filled and dotted brown boxes.

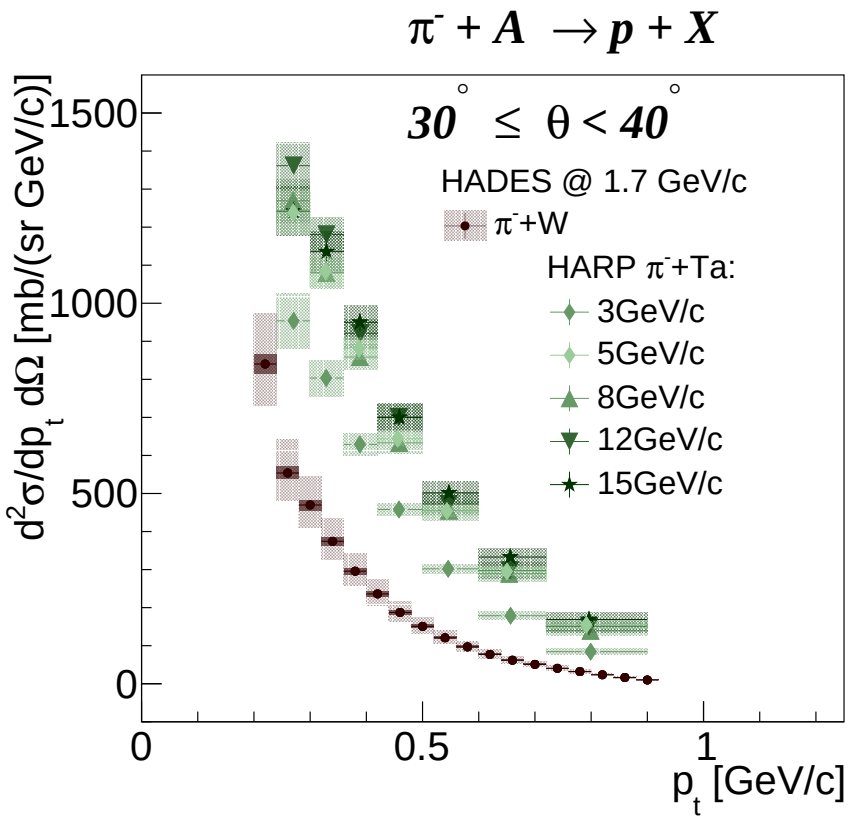

Figure 4.28: Comparison of the double-differential cross-section for polar angle region $30° < \theta < 40°$ in $\pi^- + \mathrm{W}$ (brown dots) reaction at 1.7 GeV/c with $\pi^- + \mathrm{Ta}$ at 3 GeV/c (boxes), 5 GeV/c (diamonds), 8 GeV/c (triangles), 12 GeV/c (mirrored triangles) and 15 GeV/c (stars). The statistic, systematic and normalization uncertainties are given by error bars, filled and dotted brown boxes.

5 Conclusion

In this work, the inclusive proton production cross-sections in $\pi^- + \mathrm{C}$ and $\pi^- + \mathrm{W}$ reactions at an incident beam momentum of 1.7 GeV/c, measured with HADES at SIS 18/GSI was presented.

In both collision systems, the integrated differential proton production cross-section $\Delta\sigma$ in $\pi^- + \mathrm{C}$ $(0 < y < 1.0)$ and in $\pi^- + \mathrm{W}$ $(0 < y < 0.9)$ reactions inside the HADES acceptance was obtained (Table 4.2).

In both Figures 4.21 and 4.22 a comparison to the state-of-the-art transport model calculations, performed with GiBUU and UrQMD, were presented in terms of p_t and y. For both models in both collision systems, the shape and yield look very similar except for target rapidies $(0.0 \leq y < 0.2)$. In this region, the Boltzmann extrapolation for low transverse momenta, does not match the shape of both transport model calculations. In the target rapidity region in $(\pi^- + \mathrm{C})$ reactions at small transverse momenta, the yield for GiBUU is much higher than for UrQMD. For $\pi^- + \mathrm{W}$ reactions it is the other way around. Here, the yield for GiBUU at low transverse momenta shows also a kind of double peak structure. In mid-rapidity the shape and production yield of the experimental double-differential cross-sections is reproduced by both models. Going to higher rapidity, the simulated GiBUU and UrQMD data develop a second peak, at high p_t values. The creation of this second peak indicates elastic proton scattering. In UrQMD elastic scattering is caused by the strong decay of intermediated resonaces. However, the experimental data shows no evidence for the creation of a second peak. In Figure 4.23 the comparison of the proton production cross-section as a function of rapidity to both models was shown. The shape of the experimental data in $\pi^- + \mathrm{C}$ reaction is reproduced by GiBUU and UrQMD. Both peaks (GiBUU and UrQMD) are shifted more towards target rapidity. In $\pi^- + \mathrm{W}$ reactions only GiBUU reproduces the shape of the experimental data, while UrQMD has a double peak structure at the target rapidity region. At rapidity $y > 0.2$ $(y > 0.4)$ for $\pi^- + C$ ($\pi^- + W$) reactions the shape and height is reproduced by both models.

Moreover, comparisons to the double-differential proton production cross-sections, measured by the HARP Collaboration, were presented. The double-differential proton production cross-sections for $\pi^- + \mathrm{C}$ reactions at 1.7 GeV/c, obtained in this thesis, are a

smaller than for the HARP data at 3 GeV/c at small polar angles. Going to larger polar angles and reaching higher traverse momenta, the data points are in good agreement with the HARP data. The obtained results allow to investigate the dependency of the incoming beam momenta and the proton production on the atomic number A. In Figure 4.26 for $\pi^- + \mathrm{C}$ reactions an insignificant dependency of the incident beam momentum is visible. The beam momentum dependency gets more distinct for beam reactions on heavier targets e.g. Tantalum (Fig. 4.28). Reaching higher transverse momenta, the incoming beam momentum dependency gets less distinct.

The presented measurement in this thesis is at a lower incident beam momentum (1.7 GeV/c) than HARP. Besides, a tungsten target was used in the HADES pion beam campaign, which is not included in the HARP report. So the existing HARP data could be enlarged with both, the lower incoming beam momentum and additional double differential proton production cross-section in $\pi^- + \mathrm{W}$ reactions.

List of Figures

List of Tables

Bibliography

[1] J. Adamczewski-Musch et al. A facility for pion-induced nuclear reaction studies with HADES. *Eur. Phys. J.*, A53(9):188, 2017.

[2] G. Agakishiev et al. The High-Acceptance Dielectron Spectrometer HADES. *Eur. Phys. J.*, A41:243–277, 2009.

[3] S. A. Bass et al. Microscopic models for ultrarelativistic heavy ion collisions. *Prog. Part. Nucl. Phys.*, 41:255–369, 1998. [Prog. Part. Nucl. Phys.41,225(1998)].

[4] M. Bleicher et al. Relativistic hadron hadron collisions in the ultrarelativistic quantum molecular dynamics model. *J. Phys.*, G25:1859–1896, 1999.

[5] A. Bolshakova, I. Boyko, G. Chelkov, D. Dedovitch, A. Elagin, D. Emelyanov, M. Gostkin, A. Guskov, Z. Kroumchtein, and et al. Cross-sections of large-angle hadron production in proton– and pion–nucleus interactions vi: carbon nuclei and beam momenta from ±3 gev/c to ±15 gev/c. *The European Physical Journal C*, 70(3):573–633, Nov 2010.

[6] A. Bolshakova et al. Cross-Sections of Large-Angle Hadron Production in Proton- and Pion-Nucleus Interactions. III. Tantalum Nuclei and Beam Momenta from +-3 GeV/c to +-15 GeV/c. *Eur. Phys. J.*, C63:549–609, 2009.

[7] A. Bolshakova et al. Cross-sections of large-angle hadron production in proton and pion-nucleus interactions IV: Copper nuclei and beam momenta from +-3- GeV/c to +-15-GeV/c. *Eur. Phys. J.*, C64:181–241, 2009.

[8] A. E. Bolshakova. Cross sections of large-angle hadron production in proton-nucleus and pion-nucleus interactions. *Physics of Particles and Nuclei Letters*, 9(9):755–757, Dec 2012.

[9] O. Buss, T. Gaitanos, K. Gallmeister, H. van Hees, M. Kaskulov, O. Lalakulich, A. B. Larionov, T. Leitner, J. Weil, and U. Mosel. Transport-theoretical Description of Nuclear Reactions. *Phys. Rept.*, 512:1–124, 2012.

[10] S. Chatrchyan et al. Observation of a New Boson at a Mass of 125 GeV with the CMS Experiment at the LHC. *Phys. Lett.*, B716:30–61, 2012.

[11] W. N. Cottingham and D. A. Greenwood. *An introduction to the standard model of particle physics*. Cambridge Univ. Press, Cambridge, 1998.

[12] J. Diaz et al. Design and commissioning of the GSI pion beam. *Nucl. Instrum. Meth.*, A478:511–526, 2002.

[13] L. Fabbietti. Lecture slides: Hadron physics at accellerators: Symmetries and neutron stars. Research report, Physik Department Technische Universität München, 2017.

[14] I. Fröhlich et al. A General Purpose Trigger and Readout Board for HADES and FAIR-Experiments. *IEEE Trans. Nucl. Sci.*, 55:59–66, 2008.

[15] Gibuu the giessen boltzmann-uehling-uhlenbeck project. `https://gibuu.hepforge.org/`. Reviewed at 03.02.2019.

[16] Hades. `https://www-hades.gsi.de/`. Reviewed at 18.12.2019.

[17] A. Leonidov, M. Nardi, and H. Satz. Hadron spectra from nuclear collisions. *Zeitschrift für Physik C Particles and Fields*, 74(3):535–540, Sep 1997.

[18] S. Maurus. *Λ and K^0_S Production in Pion-Nucleus Reactions at 1.7 GeV/c*. Dissertation, Technische Universität München, München, 2019.

[19] P. Salabura, J. Stroth, and L. Fabbietti. The HADES Pion Beam Facility. *Nucl. Phys. News*, 25(2):22–24, 2015.

[20] S. Sarkar, H. Satz, and B. Sinha. The physics of the quark-gluon plasma. *Lect. Notes Phys.*, 785:pp.1–369, 2010.

[21] H. Schuldes. *Charged kaon and ϕ reconstruction in Au+Au collisions at 1.23 AGeV*. PhD thesis, Goethe U., Frankfurt (main), 2016.

[22] Standardmodell. `https://de.wikipedia.org/wiki/Standardmodell/`. Reviewed at 05.12.2019.

[23] M. e. a. Tanabashi. Review of particle physics. *Phys. Rev. D*, 98:030001, Aug 2018.

[24] W. Weise. Nuclear aspects of chiral symmetry. *Nuclear Physics A*, 553:59 – 72, 1993.

[25] J. Wirth, L. Fabbietti, R. Lalik, L. Maier, and A. Scordo. CERBEROS: A tracking system for secondary pion beams at the HADES spectrometer. *Nucl. Instrum. Meth.*, A824:243–244, 2016.

[26] J. K. Wirth. *(Strange) Meson Production in Pion-Nucleus Collisions at 1.7 GeV/c*. Dissertation, Technische Universität München, München, 2019.

[27] J. Xu et al. Understanding transport simulations of heavy-ion collisions at 100A and 400A MeV: Comparison of heavy-ion transport codes under controlled conditions. *Phys. Rev.*, C93(4):044609, 2016.